nature cell biology

Friction forces position the neural anlage

Michael Smutny[1], Zsuzsa Ákos[2], Silvia Grigolon[3], Shayan Shamipour[1], Verena Ruprecht[4,5], Daniel Čapek[1], Martin Behrndt[1], Ekaterina Papusheva[1], Masazumi Tada[6], Björn Hof[1], Tamás Vicsek[2], Guillaume Salbreux[3] and Carl-Philipp Heisenberg[1,7]

During embryonic development, mechanical forces are essential for cellular rearrangements driving tissue morphogenesis. Here, we show that in the early zebrafish embryo, friction forces are generated at the interface between anterior axial mesoderm (prechordal plate, ppl) progenitors migrating towards the animal pole and neurectoderm progenitors moving in the opposite direction towards the vegetal pole of the embryo. These friction forces lead to global rearrangement of cells within the neurectoderm and determine the position of the neural anlage. Using a combination of experiments and simulations, we show that this process depends on hydrodynamic coupling between neurectoderm and ppl as a result of E-cadherin-mediated adhesion between those tissues. Our data thus establish the emergence of friction forces at the interface between moving tissues as a critical force-generating process shaping the embryo.

Throughout embryonic development, tissue morphogenesis depends on mechanical forces that drive cell rearrangements and global tissue shape changes[1,2]. In zebrafish gastrulation, epiboly, internalization, convergence and extension constitute the main cellular processes by which the embryo takes shape[3]. Although recent studies have unravelled key force-generating mechanisms mediating these different cellular processes[3], how forces between neighbouring tissues are generated, perceived and integrated is yet poorly understood.

Development of the central nervous system in vertebrates involves extensive morphogenetic movements within the embryonic neurectoderm[4]. The zebrafish nervous system organization becomes first apparent at gastrulation[5], and morphogenesis of the neurectoderm is accompanied by neighbouring tissues undergoing dynamic cellular reorganization[6]. Recent studies in zebrafish suggested that the formation of the mesoderm and endoderm (mesendoderm) germ layers is required for proper morphogenesis of the overlying neurectoderm during neural keel formation[7,8]. However, the mechanisms by which mesendoderm influences neurectoderm morphogenesis have only started to be unravelled.

RESULTS

Anterior axial mesendoderm (prechordal plate) collective cell migration affects neurectoderm morphogenesis

To investigate the role of mesendoderm in neurectoderm morphogenesis (for tissue organization within the gastrulating embryo, see Fig. 1), we turned to zebrafish maternal zygotic (MZ) *one-eyed-pinhead* (*oep*) mutant embryos[9], which lack much of the mesendoderm germ layers due to defective Nodal/TGF β-signalling. Interestingly, when analysing MZ*oep* mutants at late stages of gastrulation, we found that the anterior neural anlage was positioned closer to the vegetal pole than in wild-type (wt) embryos (Fig. 2a,b,i,j and Supplementary Fig. 2k–m). This points at the intriguing possibility that mesendoderm is required for proper positioning of the anterior neural anlage. To further test this possibility, we analysed how the neurectoderm, which gives rise to the anterior neural anlage, interacts with the underlying anterior axial mesendoderm (prechordal plate, ppl) during gastrulation. Previous studies have suggested that the ppl moves as a migrating cell collective in a straight path towards the animal pole, while the neurectoderm moves in the opposite direction towards the vegetal pole (Fig. 1a–e)[10]. To understand how these in opposite directions moving tissues might influence each other, we first analysed the localization of molecules involved in cell–cell and cell–extracellular matrix (ECM) adhesion at the neurectoderm/ppl interface. We found that the cell–cell adhesion receptor E-cadherin accumulated at the interface between ppl and neurectoderm during gastrulation (Fig. 1f), supporting previous observations that ppl and neurectoderm cells form E-cadherin-mediated cell–cell contacts at this interface[10]. In contrast, ECM components, such as fibronectin, did not show any recognizable accumulations at the neurectoderm/ppl interface until late stages of gastrulation (Supplementary Fig. 1a–c),

[1]Institute of Science and Technology Austria, Am Campus 1, A-3400 Klosterneuburg, Austria. [2]Department of Biological Physics, Eötvös University, Pázmány Péter sétány 1A, Budapest H-1117, Hungary. [3]The Francis Crick Institute, 1 Midland Road, London NW1 1AT, UK. [4]Centre for Genomic Regulation (CRG), The Barcelona Institute for Science and Technology, Dr. Aiguader 88, 08003 Barcelona, Spain. [5]Universitat Pompeu Fabra (UPF), 08003 Barcelona, Spain. [6]Department of Cell and Developmental Biology, University College London, Gower Street, London WC1E 6BT, UK. [7]Correspondence should be addressed to C.-P.H. (e-mail: heisenberg@ist.ac.at)

Received 21 October 2016; accepted 17 February 2017; published online 27 March 2017; DOI: 10.1038/ncb3492

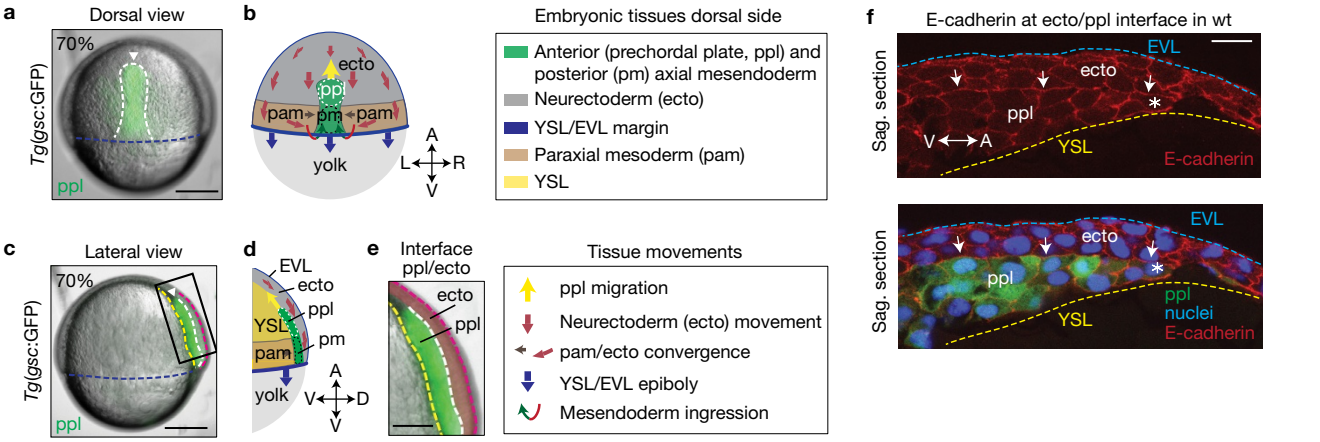

Figure 1 Neurectoderm (ecto) and prechordal plate (ppl) morphogenesis during gastrulation. (**a**,**c**) Bright-field/fluorescence images of a *Tg*(*gsc*:GFP) zebrafish embryo at 7.0 hpf; GFP-labelled ppl leading edge cells are indicated (white arrowheads); the rectangle in **c** marks the magnified area in **e**; the dashed lines in **a** indicate axial mesendoderm (white), and in **c** ecto-to-ppl (white), yolk syncytial layer (YSL)-to-ppl (yellow), enveloping layer (EVL)-to-media (pink) and EVL-to-YSL (blue) interfaces; embryonic axis orientation as marked in **b**,**d** for same views. (**b**,**d**) Illustration of embryonic (anterior (ppl) and posterior axial mesendoderm (pm), paraxial mesoderm (pam) and ecto) and extra-embryonic (YSL, EVL, yolk) tissues, and their respective direction of movement during gastrulation at the dorsal side of the zebrafish embryo; arrows in **b**,**d** indicate animal–vegetal (A–V), left–right (L–R) and dorsal–ventral (D–V) embryonic axes. (**e**) A magnified view of the boxed area in **c** showing neighbouring ppl (green) and overlying ecto (red pseudocoloured) tissues; dashed lines as in **c**. (**f**) Immunofluorescence confocal images of sagittal sections of the ecto-to-ppl interface at 7.5 hpf stained for E-cadherin (upper panel) and merged with ppl progenitors expressing *gsc*:GFP and DAPI-stained nuclei (lower panel); the arrows highlight E-cadherin accumulations at the ecto-to-ppl interface, and asterisks mark ppl leading edge cells; the blue dashed line indicates the EVL-to-media interface, and the yellow dashed line outlines ppl- and ecto-to-YSL interfaces; animal pole to the right. All embryos animal pole up; dorsal (**a**,**b**) and lateral (**c**–**f**) views with dorsal right. Scale bars, 200 μm (**a**,**c**), 100 μm (**e**), and 20 μm (**f**).

arguing against ECM playing an important role in mediating the interaction between ppl and neurectoderm cells during early stages of gastrulation[11]. Consistent with ppl and neurectoderm cells forming E-cadherin-mediated cell–cell contacts, we also found interstitial fluid accumulations to be absent from places where E-cadherin accumulates at the neurectoderm/ppl interface (Supplementary Fig. 1d). Collectively, these observations suggest that neurectoderm and ppl constitute two directly adjacent tissues that globally move in opposite directions during gastrulation and contact each other directly at their interface via E-cadherin-mediated cell–cell adhesions.

Next we asked whether neurectoderm movements towards the vegetal pole might be influenced by the underlying ppl migrating in the opposite direction towards the animal pole of the embryo. To this end, we compared neurectoderm cell movements in wt embryos forming a ppl versus MZ*oep* mutant embryos defective in ppl formation (Supplementary Fig. 2a,i and Supplementary Videos 1 and 2). For quantifying neurectoderm cell movements relative to the movement of ppl cells, we constructed two-dimensional (2D) cellular flow maps of velocities and directions from 3D tracking data (Fig. 2c). Consistent with previous observations[10,12,13], we found that ppl progenitors migrated in a highly coordinated and directed manner towards the animal pole of the wt gastrula (Supplementary Fig. 2b–d). Remarkably, while the bulk of neurectoderm cells in wt underwent epiboly movements directed towards the vegetal pole, cells located directly above and anterior to the leading edge of the ppl slowed down their vegetal-directed movement and reoriented their direction of motion from vegetal to animal (Fig. 2c,d and Supplementary Fig. 2e,f and Supplementary Video 3), resulting in high animal-directed movement alignment with the adjacent ppl progenitors (measured average local correlation (C_L) over time interval (t, min) $C_{L(t120)} = 0.37 \pm 0.03$ (s.e.m., $n = 6$ embryos); Fig. 2e,f and Supplementary Fig. 2g,h and Supplementary Video 4). This local reorientation of neurectoderm cell movements close to the leading edge of the ppl in wt was accompanied by the formation of characteristic large-scale cell flows within the neurectoderm resembling two counter-rotating vortices, which were mirrored along the embryo midline (Fig. 2c,g,h and Supplementary Video 3). Notably, there was only little influence on the movements of neurectoderm cells posterior of the ppl, probably due to posterior axial mesendoderm behind the ppl displaying much less pronounced animal-directed movements (Supplementary Fig. 1e,f). In contrast to the situation in wt embryos, neurectoderm cells in MZ*oep* embryos lacking ppl progenitors (Supplementary Fig. 2i) showed none of the characteristic flow patterns found in wt and, instead, moved exclusively towards the vegetal pole (Fig. 1k–n and Supplementary Fig. 2j and Supplementary Video 5). Collectively, these observations point to the possibility that animal-directed migration of ppl cells reorient the vegetal-directed movement of adjacent neuroectoderm cells.

Movement speed of neurectoderm and prechordal plate (ppl) controls neurectoderm morphogenesis

To determine whether changing ppl cell movement would affect neurectoderm cell rearrangements, we turned to *slb/wnt11* morphant embryos (Fig. 3a), in which ppl cells move less coordinated and slower towards the animal pole due to compromised expression of the non-canonical Wnt ligand Wnt11 (Supplementary Fig. 3e–h)[14,15]. When analysing cell movements in *slb* morphants, we found that neurectoderm cells located above and ahead of the ppl displayed increased vegetal-directed movements, and that the characteristic vortex movements within the neurectoderm were largely lost

(Fig. 3b,c). Moreover, the alignment of neurectoderm with ppl cell movements was strongly diminished ($C_{L(t120)} = -0.24 \pm 0.04$ (s.e.m., $n = 4$ embryos); Fig. 3d,e) and, importantly, the anterior neural anlage was positioned closer to the vegetal pole compared with wt embryos (Fig. 3p,q and Supplementary Fig. 3j,k). Notably, similar effects were observed in *cyclops/ndr2* (*cyc*) mutant embryos (Fig. 3f), in which a diminished number of ppl cells due to compromised expression of the Nodal signal Ndr2[16,17] displayed reduced velocity and less coordinated movements (Supplementary Fig. 3a–d). This resulted in increased vegetal-directed movements of neurectoderm cells close to the ppl (Fig. 3g,h), decreased movement alignment between ppl and the neurectoderm ($C_{L(t120)} = -0.035 \pm 0.027$ (s.e.m., $n = 3$ embryos); Fig. 3i,j) and a more vegetal localization of the neural anlage along the animal–vegetal (AV) axis compared with wt embryos (Fig. 3p,q and Supplementary Fig. 3i,k). Collectively, these observations strongly support the notion that proper animal-directed collective ppl cell migration is critical for normal neurectoderm cell movements and positioning of the neural anlage (Fig. 3r).

Next, we asked whether epiboly movements of neurectoderm cells towards the vegetal pole are also important for ppl cells to control neurectoderm morphogenesis. To reduce epiboly movements, we overexpressed a constitutively active version of the myosin-II phosphatase (CA-Mypt) specifically within the yolk syncytial layer (YSL) (Fig. 3k and Supplementary Fig. 4a–c)[18]. In CA-Mypt-overexpressing embryos, animal-directed movements of neurectoderm cells were more pronounced (Fig. 3l,m), whereas ppl cell migration remained unchanged (Supplementary Fig. 4d–h). Moreover, the degree of alignment between ppl and neurectoderm movements was enhanced ($C_{L(t120)} = 0.61 \pm 0.02$ (s.e.m., $n = 4$ embryos); Fig. 3n,o and Supplementary Video 6), and the anterior neural anlage was positioned closer to the animal pole (Fig. 3p,q and Supplementary Fig. 4i,j). This suggests that the effect of ppl cell movements on neurectoderm morphogenesis becomes more apparent when neurectoderm epiboly movements are reduced (Fig. 3r).

Continuous mesendoderm cell ingression is required for ppl cells affecting neurectoderm morphogenesis

Movement of ppl cells towards the animal pole is initiated by the synchronized ingression of ppl progenitors at the dorsal germ ring margin[10]. To test whether continuous ingression of mesendoderm progenitors is required for animal-directed ppl cell migration and, consequently, their effect on neurectoderm cell movements, we analysed ppl and neurectoderm cell movements in the absence of mesendoderm cell ingression. To this end, we transplanted 100–150 induced ppl progenitor cells[19] below the neurectoderm close to the dorsal germ ring margin of MZ*oep* embryos lacking endogenous mesendoderm cell ingression[9] and monitored their movement relative to adjacent neurectoderm cells (Fig. 4a and Supplementary Fig. 5a–c,e). Although most of the transplanted cells displayed protrusions directed towards the animal pole (Supplementary Fig. 5d), their movement coordination and directed migration were severely impaired (Supplementary Fig. 5f,g). This is consistent with previous suggestions that anchorage of ppl progenitors to newly internalizing cells at their rear is required for their animal-directed migration[20]. Notably, neurectoderm cells adjacent to the transplanted ppl progenitors showed vegetal-directed movements indistinguishable from neurectoderm cells in non-transplanted MZ*oep* mutant embryos (Fig. 4b,c and Supplementary Video 7). Moreover, as gastrulation proceeded, transplanted ppl cells started to move towards the vegetal pole in the same direction as the overlying neurectoderm cells, resulting in highly aligned vegetal-directed movements of neurectoderm and transplanted ppl cells ($C_L = 0.48 \pm 0.04$ (s.e.m. $n = 3$ embryos); Fig. 4d,e).

To test whether slowing down neurectoderm epiboly movements would restore ppl-induced redirection of neurectoderm cells, we reduced the speed of vegetal-directed neurectoderm cell movements in transplanted MZ*oep* mutant embryos by overexpressing CA-Mypt specifically within the YSL of those embryos (Fig. 4f and Supplementary Fig. 5h–k) and monitored the interaction between transplanted ppl cells and adjacent neurectoderm cells. We found that ppl cells showed increased animal-directed movements when vegetal-directed neurectoderm cell movements were slowed down in MZ*oep* embryos (Fig. 4g,h and Supplementary Video 8). Moreover, neurectoderm cells adjacent to the transplanted ppl cells transiently reoriented their movement towards the animal pole (Fig. 4h), resulting in temporary high animal-directed movement alignment between transplanted ppl and adjacent neurectoderm cells ($C_{L(t80)} = 0.53 \pm 0.04$ (s.e.m., $n = 3$ embryos); Fig. 4i,j). These observations strongly support the notion that the difference in movement speed along the AV axis between ppl and neurectoderm cells determines whether ppl influences neurectoderm cell movements or *vice versa*.

Friction forces between neurectoderm and ppl mediate the effect of ppl on neurectoderm morphogenesis

We hypothesized that the observed large-scale cellular rearrangements within the neurectoderm might be generated by friction forces arising at the tissue interface between ppl and neurectoderm. To test this hypothesis, we formulated a theoretical model based on the physical principles of viscous fluid motion at low Reynolds numbers (Supplementary Note). In this model, we considered the neurectoderm as a thin layer of viscous compressible fluid exposed to external friction arising at its interface with EVL and/or yolk cell and being in contact with ppl cells, which were modelled as a rectangular element exerting a friction force on the neurectoderm (Supplementary Note).

We first aimed at comparing neurectoderm velocity profiles along the animal–vegetal axis with a simplified, effectively 1D theory (Fig. 5a). To assess the effect of ppl cells on neurectoderm movement, we measured unperturbed neurectoderm epiboly movements in MZ*oep* mutants devoid of ppl cells and subtracted those epiboly movements from the overall neurectoderm flow field in wt embryos (Supplementary Fig. 6a). Consistent with our experimental observations (Fig. 5b), we assumed that the velocity of the calculated neurectoderm flow vanishes at the ventral and dorsal margins of the neurectoderm in both the presence and absence of the ppl. In our model, the external friction force acting outside the ppl domain causes the velocity profile to decay exponentially away from ppl cells, on a length scale that decreases when the friction coefficient increases (Supplementary Note), while in the absence of such external friction, this decay is linear (Supplementary Fig. 6b). When performing a fit to experimentally obtained neurectoderm flow profiles in wt, we obtained a very close agreement between the calculated and experimentally observed flow profiles for a very low external friction force (Fig. 5b and Supplementary Fig. 6c).

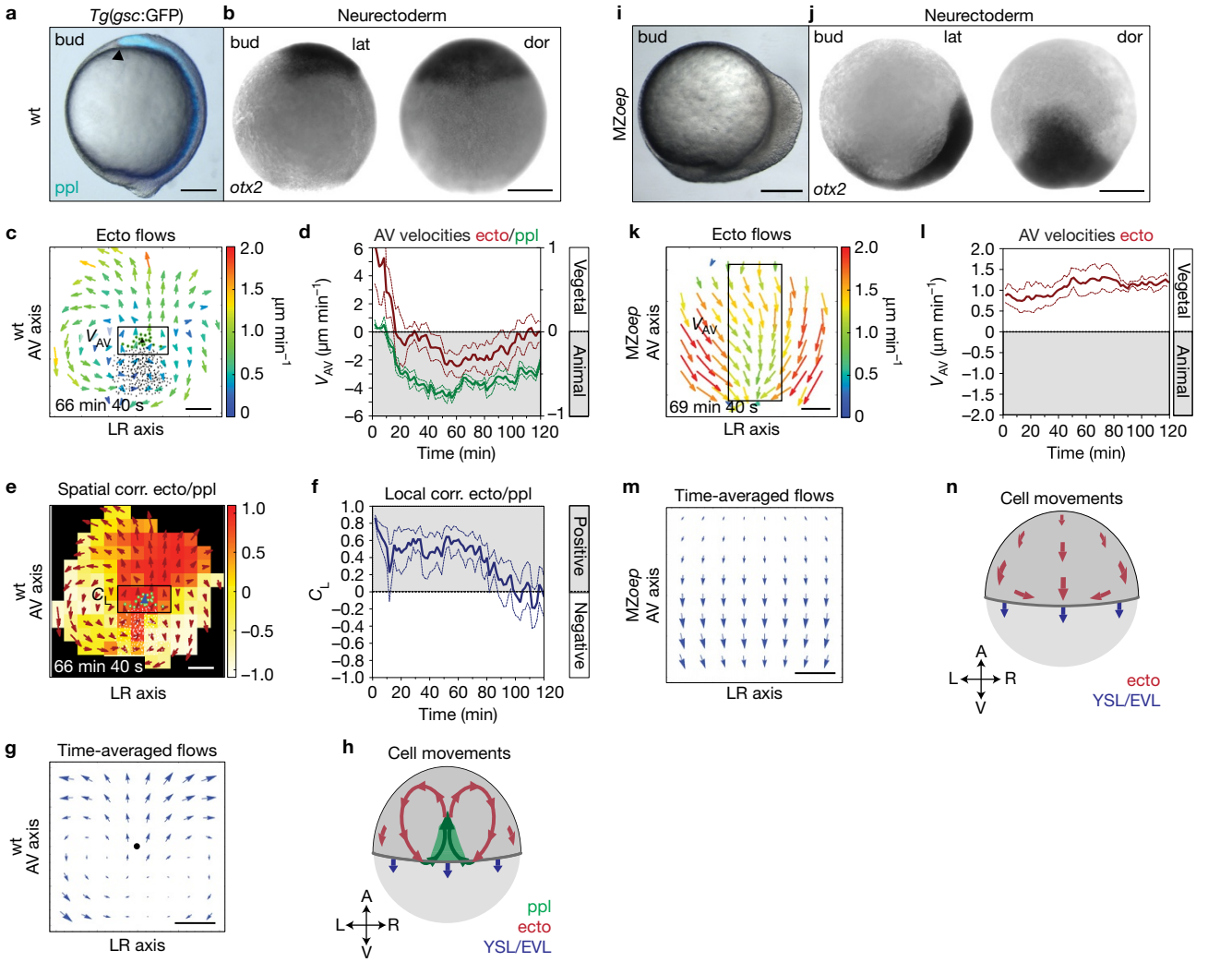

Figure 2 Defective neurectoderm (ecto) morphogenesis in MZ*oep* mutants. (**a**,**i**) Bright-field/fluorescence images of *Tg*(*gsc*:GFP) wt (**a**) and MZ*oep* mutant embryos (**i**) at the end of gastrulation (bud stage, 10 hpf); the arrowhead in **a** marks the anterior edge of GFP (blue)-labelled ppl. (**b**,**j**) Anterior neurectoderm progenitor cells in a wt (**b**) and MZ*oep* embryo (**j**) at bud stage (10 hpf) visualized by whole-mount *in situ* hybridization of *otx2* mRNA. (**c**,**k**) 2D tissue flow map indicating average velocities of ecto movements along the animal–vegetal (AV) and left–right (LR) axis at the dorsal side of a wt (**c**; 7.1 hpf) and MZ*oep* embryo (**k**; 7.2 hpf); local average ecto velocities colour-coded ranging from 0 (blue) to 2 (red) μm min^{-1}; positions of all/leading edge ppl cells marked by black/green dots; boxed areas are used for measurements in **d**,**l**. (**d**,**l**) Mean velocities along the AV axis (V_{AV}) of ecto (red; right *y* axis; boxed area in **c**,**k**) and underlying ppl leading edge cells (green, left *y* axis) in wt (**d**; $n=6$ embryos) and MZ*oep* embryos (**l**; $n=4$ embryos); 6–8 hpf; error bars (dashed lines), s.e.m. (**e**) 3D directional correlation between ecto and ppl in a wt embryo at 7.1 hpf; colour-coded correlation ranging from 1 (red, highest) to −1 (white, lowest); red arrows indicate local averaged ecto velocities; position of all/leading edge ppl cells marked by white/green dots; blue arrowhead indicates average velocity of ppl leading edge cells; boxed area was used for measurements in **f**. (**f**) 3D average directional correlation between leading edge ppl and adjacent neurectoderm cells (black boxed area in **e**) used for local correlation (C_L) calculation in wt embryos ($n=6$ embryos); 6–8 hpf; error bars (dashed lines), s.e.m. (**g**,**m**) 2D tissue flow map of ecto cells showing time-averaged velocities (over 120 min from 3 embryos) along the AV and LR axes at the dorsal side in wt (**g**) and MZ*oep* embryos (**m**); black dot in **g** marks position of ppl leading edge. (**h**,**n**) Schematic of ecto (red), ppl (green), and enveloping layer (EVL)/yolk syncytial layer (YSL) movements (blue) in wt (**h**) and MZ*oep* embryos (**n**); arrows indicate AV and LR embryonic axes. All embryos animal pole up; dorsal (**b**,**j** (dor) and **h**,**n**) and lateral (**a**,**i** and **b**,**j** (lat)) views with dorsal right. Scale bars, 200 μm (**a**,**b**,**g**,**i**,**j**) and 100 μm (**c**,**e**,**k**,**m**).

Next, we extended our analysis to *slb* morphant embryos, where the effect of changing the relative velocity between neuroectoderm and ppl cells was clearly detectable throughout the time frame of our analysis (6–8 hours post fertilization (hpf)). When analysing *slb* morphant embyros, we made the assumption that if the ppl cells were to exert a dynamic friction force that is linearly dependent on the relative velocities between the two tissues, we would expect the force to be decreased by the same amount as the relative velocity between neurectoderm and ppl (20% reduction). Indeed, we found that calculated neurectoderm flow profiles with a ppl friction force reduced by 20% (Supplementary Note and Supplementary Table 1) closely resembled the experimentally obtained flow profiles in *slb* morphants (Fig. 5b1). Together, our 1D analysis of neurectoderm flows in wt and *slb* morphant embryos revealed a remarkable quantitative similarity between the model predictions and experimental observations, supporting the notion that friction forces mediate the effect of ppl on neurectoderm motion.

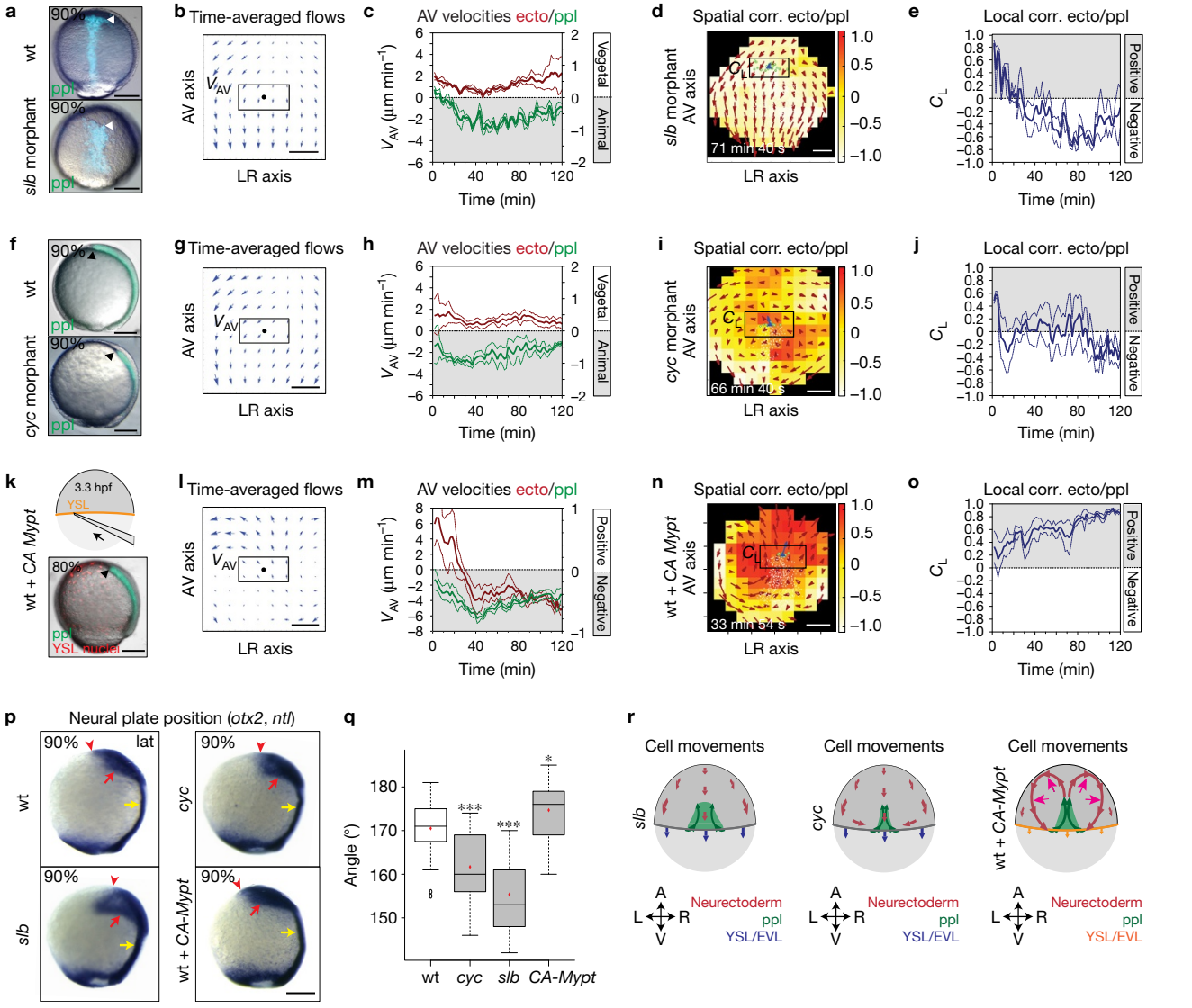

Figure 3 Prechordal plate (ppl) velocity determines the effect of ppl on neurectoderm (ecto) morphogenesis. (**a**,**f**,**k**) Bright-field/fluorescence images of a *Tg*(*gsc*:GFP) wt (**a**,**f**; top panel), *slb* (**a**; bottom panel) and *cyc* morphant embryo (**f**, bottom panel) at 9 hpf; *Tg*(*gsc*:GFP) embryo (**k**) injected at 3.3 hpf with *CA-Mypt* and *H2A-mCherry* mRNAs into the YSL (top panel, schematic) at 8 hpf; arrowheads, GFP (green/blue)-labelled ppl leading edge. (**b**,**g**,**l**) 2D tissue flow map of time-averaged velocities of ecto cells (over 120 min, 3 embryos) along animal–vegetal (AV) and left–right (LR) axes at the dorsal side of *slb* (**b**), *cyc* (**g**) and *CA-Mypt*-injected embryos (**l**); black dots; ppl leading edge positions; boxed areas used for measurements in **c**,**h**,**m**. (**c**,**h**,**m**) Mean velocities along the AV axis (V_{AV}) of ecto (red; right *y* axis; boxed areas in **b**,**g**,**l**) and underlying leading edge ppl cells (green, left *y* axis) in *slb* (**c**; $n=4$ embryos), *cyc* (**h**; $n=3$ embryos) and *CA-Mypt*-injected embryos (**m**; $n=4$ embryos); 6–8 hpf; error bars (dashed lines), s.e.m. (**d**,**i**,**n**) 3D directional correlation map between ecto and ppl cells in a *slb* (**d**; 7.1 hpf), *cyc* (**i**; 7.2 hpf) and *CA-Mypt*-injected embryo (**n**; 6.6 hpf); colour-coded correlation ranging from 1 (red, highest) to −1 (white, lowest); red arrows, local averaged ecto velocities; position of all/leading edge ppl cells marked by white/green dots; blue arrowhead indicates average velocity of ppl leading edge cells; boxed areas used for measurements in **e**,**j**,**o**. (**e**,**j**,**o**) 3D average directional correlation between leading edge ppl and ecto cells (boxed areas in **d**,**i**,**n**) in *slb* (**e**; $n=4$ embryos), *cyc* (**j**; $n=3$ embryos) and *CA-Mypt*-injected embryos (**o**; $n=4$ embryos); 6–8 hpf; error bars (dashed lines), s.e.m. (**p**) Anterior neural anlage and notochord labelled by *otx2* (red arrows) and *ntl* expression (yellow arrows), respectively, in wt, *slb*, *cyc* and *CA-Mypt*-injected embryos at 9 hpf; arrowheads denote anterior neural plate edge. (**q**) Angle (°) between the vegetal pole and neural plate anterior edge in wt, *slb*, *cyc* and *CA-Mypt*-injected embryos at 9 hpf. Student's *t*-test for all graphs; ***, $P<0.001$; *, $P<0.05$; *n* (embryos from 4 independent experiments) wt/*cyc*/*slb*/*CA-Mypt*=36(<0.001)/39(<0.001)/17(<0.0001)/22(0.0194); box plot centre, median; red dot, mean; upper whisker, maximum; lower whisker, minimum. (**r**) Schematic of ecto (red), ppl (green) and enveloping layer (EVL)/yolk syncytial layer (YSL) (blue/orange) movements in *slb*, *cyc* and *CA-Mypt*-injected (magenta arrows, increased vortex flow) embryos; arrows, AV and LR axes. All embryos animal pole up; dorsal (**f**) and lateral (lat; **a**,**k**,**p**) views with dorsal right; scale bars, 200 μm (**a**,**f**,**k**,**p**) or 100 μm (**b**,**g**,**l**,**d**,**i**,**n**).

We further asked whether our 1D description could also account for 2D neurectoderm flow patterns within the domain of observation. Since our 1D analysis revealed that external friction outside the ppl domain is very low, we neglected its contribution to neurectoderm flows in our 2D analysis. We also assumed for simplicity that the bulk and shear viscosity of the fluid are equal. We then solved the equations in the 2D rectangular domain of our experimental observations, imposing the experimentally measured

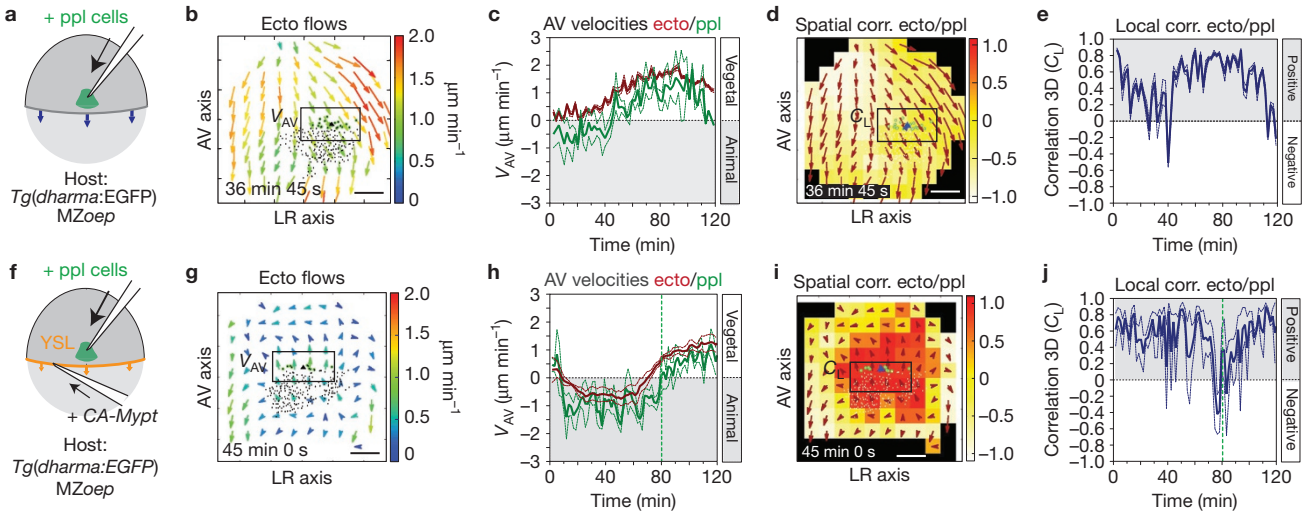

Figure 4 Mesendoderm cell ingression is required for ppl affecting ecto cell movements. (**a**,**f**) Schematic of ppl cells (green)transplanted at 6 hpf into the dorsal side of a MZ*oep* (**a**) or MZ*oep* embryo injected with *CA-Mypt* mRNA into the YSL (**f**). (**b**,**g**) 2D tissue flow map indicating average velocities of ecto movements along the animal–vegetal (AV) (V_{AV}) and left–right (LR) (V_{LR}) axis at the dorsal side of a transplanted MZ*oep* mutant (**b**; 6.6 hpf) and transplanted MZ*oep* embryo overexpressing CA-Mypt within the YSL (**g**; 6.7 hpf); local average ecto velocities indicated by arrows colour-coded ranging from 0 (blue) to 2 (red) μm min^{-1}; positions of all/leading edge transplanted ppl cells marked by black/green dots; boxed areas were used for measurements in **c**,**h**. (**c**,**h**) V_{AV} of ecto (red; boxed areas in **b**,**g**) and underlying ppl leading edge cells (green) in transplanted MZ*oep* (**c**; $n=3$ embryos) and transplanted MZ*oep* embryos overexpressing CA-Mypt within the YSL (**h**; $n=3$ embryos); 6–8 hpf; the vertical dashed line in **h** indicates the start of vegetal-directed movements of ppl cells; error bars (dashed lines), s.e.m. (**d**,**i**) 3D directional correlation between leading edge ppl and ecto cells in a transplanted MZ*oep* (**d**; 6.7 hpf) and transplanted MZ*oep* mutant embryo overexpressing CA-Mypt within the YSL (**i**; 6.7 hpf); colour-coded correlation ranging from 1 (red, highest) to −1 (white, lowest); red arrows indicate local averaged ecto velocities; position of all/leading edge ppl cells marked by white/green dots; blue arrowhead indicates average velocity of ppl leading edge cells; boxed areas were used for measurements in **e**,**j**. (**e**,**j**) 3D average directional correlation between leading edge ppl and adjacent ecto cells (boxed areas in **d**,**i**) in transplanted MZ*oep* (**e**; $n=3$ embryos) and transplanted MZ*oep* embryos overexpressing CA-Mypt within the YSL (**j**; $n=3$ embryos); 6–8 hpf; vertical dashed line (**j**) as in **h**; error bars (dashed lines), s.e.m. All scale bars, 100 μm.

velocities on the boundaries of the domain (Fig. 5c and Supplementary Note) and compared predicted to experimentally observed neurectoderm velocities. We first analysed alterations in neurectoderm movement in wt embryos displaying normal ppl cell movements. By adjusting the ratio between the force density and neurectoderm bulk viscosity (f/η_b) (Supplementary Note and Supplementary Table 1), we found that the predicted neurectoderm velocity profile in wt embryos matched well the magnitude and shape of the experimentally determined velocity profile (Fig. 5d,e,f–f3). Assuming that the force exerted by ppl cells originates from dynamic friction between these two moving tissues with a friction coefficient ξ, we further obtained the ratio of internal viscosity to friction against ppl cells η_b/ξ (Supplementary Note and Supplementary Table 1) and, given previous measurements of tissue viscosity[21], a value of the friction coefficient in the order of $\xi \sim 1$ pN s μm^{-3} (Supplementary Note). Applying the same logic to *slb* morphant embryos produced 2D neurectoderm flow patterns very closely matching the experimentally observed ones (Fig. 5d1,e1,g–g3), suggesting that the friction force density at the neurectoderm/ppl interface is critical for the effect ppl cells have on neurectoderm cell movements.

Friction forces between neurectoderm and ppl depend on transient *e-cadherin*-mediated cell–cell contacts at the tissue interface

To understand how friction can arise at this interface, we first analysed ppl cell migration and protrusive activity by visualizing the actin cytoskeleton of migrating ppl cells (Fig. 6a,b). We found that ppl cells were organized in a shingled array along the dorsal–ventral (DV) axis of the ppl (Fig. 6a,f and Supplementary Video 9) with cells at the leading edge displaying protrusions typically adhering to the YSL surface, which served as a substrate for their migration (Fig. 6b and Supplementary Video 10). Moreover, ppl progenitors close to the interface with the neurectoderm usually trailed behind cells positioned further away from this interface along the DV extent of the ppl (Fig. 6a,b and Supplementary Video 9), consistent with the possibility that friction at this interface slows down their animal-directed migration. To further test this assumption, we plotted the velocities of ppl progenitors in wt embryos along the DV axis of the ppl (Fig. 6c). We found a linear velocity gradient along this axis with its minimum at the interface to the overlying neurectoderm (Fig. 6e), as expected for friction forces at the neurectoderm/ppl interface most strongly slowing down the movement of ppl cells directly adjacent to this interface (Fig. 6f).

We then asked which molecular players might be involved in building up friction at the neurectoderm/ppl interface. Our estimation of the friction coefficient between neurectoderm and ppl cells being in the order of $\xi \sim 1$ pN s μm^{-3} (Supplementary Note) argues against the possibility of interstitial fluid alone generating this friction, given that the friction coefficient for a fluid with the viscosity of water and a layer of thickness $h = 100$ nm (corresponding to the estimated distance between ppl and neurectoderm) would be in the order of $\xi \sim 0.01$ pN s μm^{-3}. In contrast, our initial analysis indicated that the cell–cell adhesion receptor E-cadherin, unlike ECM components (Fig. 1f and Supplementary Fig. 1a), might be a likely candidate generating

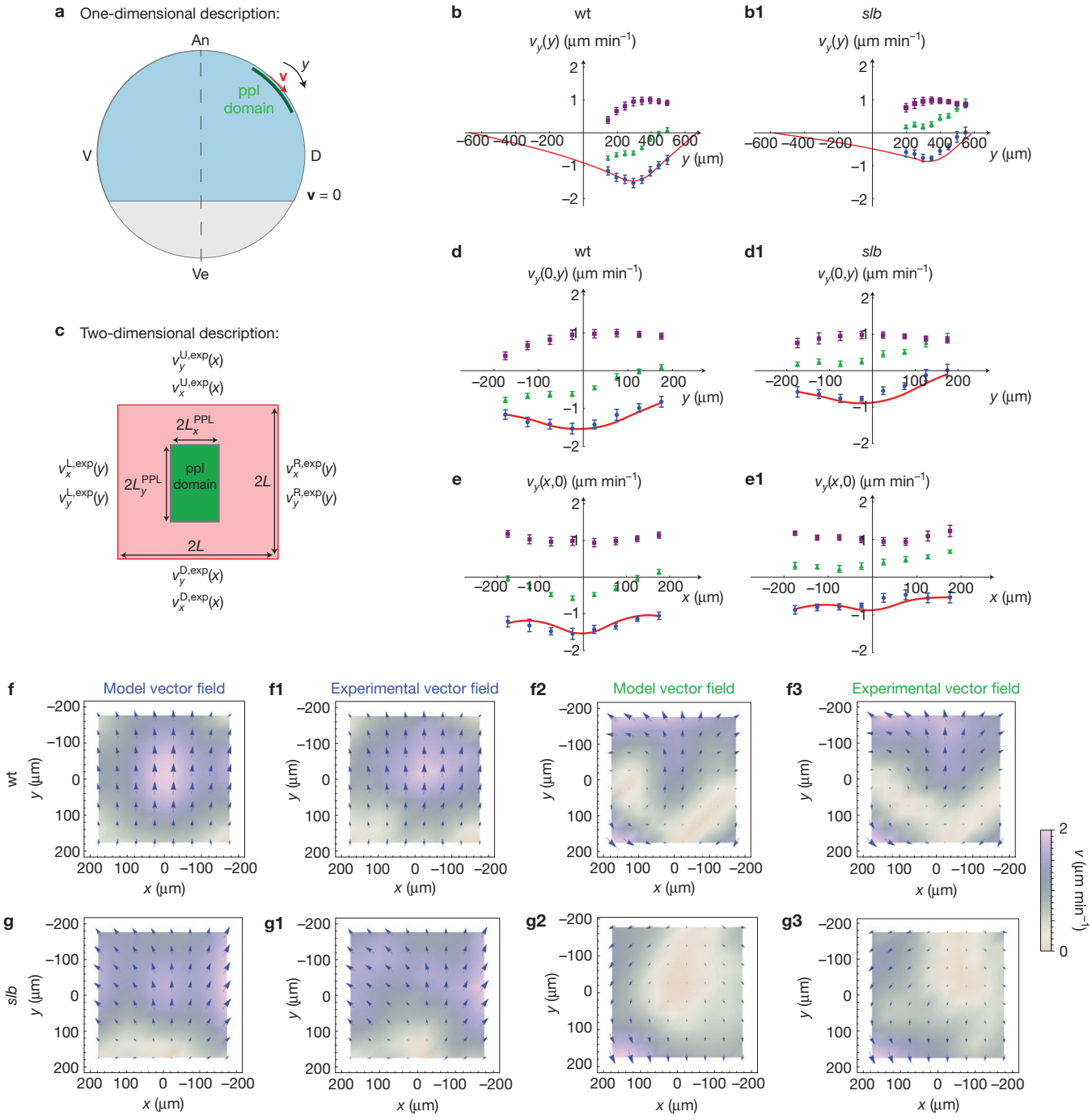

Figure 5 Hydrodynamic model description of the influence of ppl on ecto cell flows through friction forces at the tissue interface. (**a**) Illustration of 1D ecto flow description along the tissue midline axis; ppl domain exerts an animal-directed force on the ecto; the differential velocity **v** of ecto tissue equals 0 at tissue boundaries. (**b**,**b1**) 1D analysis of ecto flow velocity (v_y) along the tissue midline axis in wt (**b**) and *slb* morphant (**b1**) embryos; predicted flow profile (red), experimentally obtained flow velocities in wt and *slb* morphant embryos subtracted by the flows in MZ*oep* mutants (blue), non-subtracted flow profiles in wt and *slb* morphant embryos (green), and flows in MZ*oep* mutants (purple) are shown; values of the 1D model parameters used for each experimental case are listed in Supplementary Table 1 (Supplementary Note). (**c**) Illustration of 2D ecto flow description within the experimental image plane; velocities at the up (U), down (D), right (R) and left (L) boundaries of the image plane are taken from experimental measurements; a uniform force density is exerted on the ecto within the ppl domain. (**d**–**e1**) 2D analysis of ecto flow velocities for wt (**d**,**e**) and *slb* morphant (**d1**,**e1**) embryos; upper panels (**d**,**d1**) show the v_y velocities along the ecto tissue midline axis and lower panels (**e**,**e1**) the v_y velocities along the mediolateral extent of the ecto; colour labelling of curves as in **b**,**b1**; values of the 2D model parameters used for each experimental case are listed in Supplementary Table 1 (Supplementary Note). (**f**–**g3**) 2D vector density plots for the theoretical and experimental ecto flow velocity fields of wt (**f**–**f3**) and *slb* morphant embryos (**g**–**g3**); subtracted flow fields for wt (**f**,**f1**) and *slb* morphant (**g**,**g1**) embryos; non-subtracted total flow velocity fields for wt (**f2**,**f3**) and *slb* morphant (**g2**,**g3**) embryos generated by adding corresponding experimental MZ*oep* velocities to the theoretical flow profiles; direction (arrows) and colour-coded velocities from 0 (white, lowest) to 2 (purple, highest). All error bars s.d.

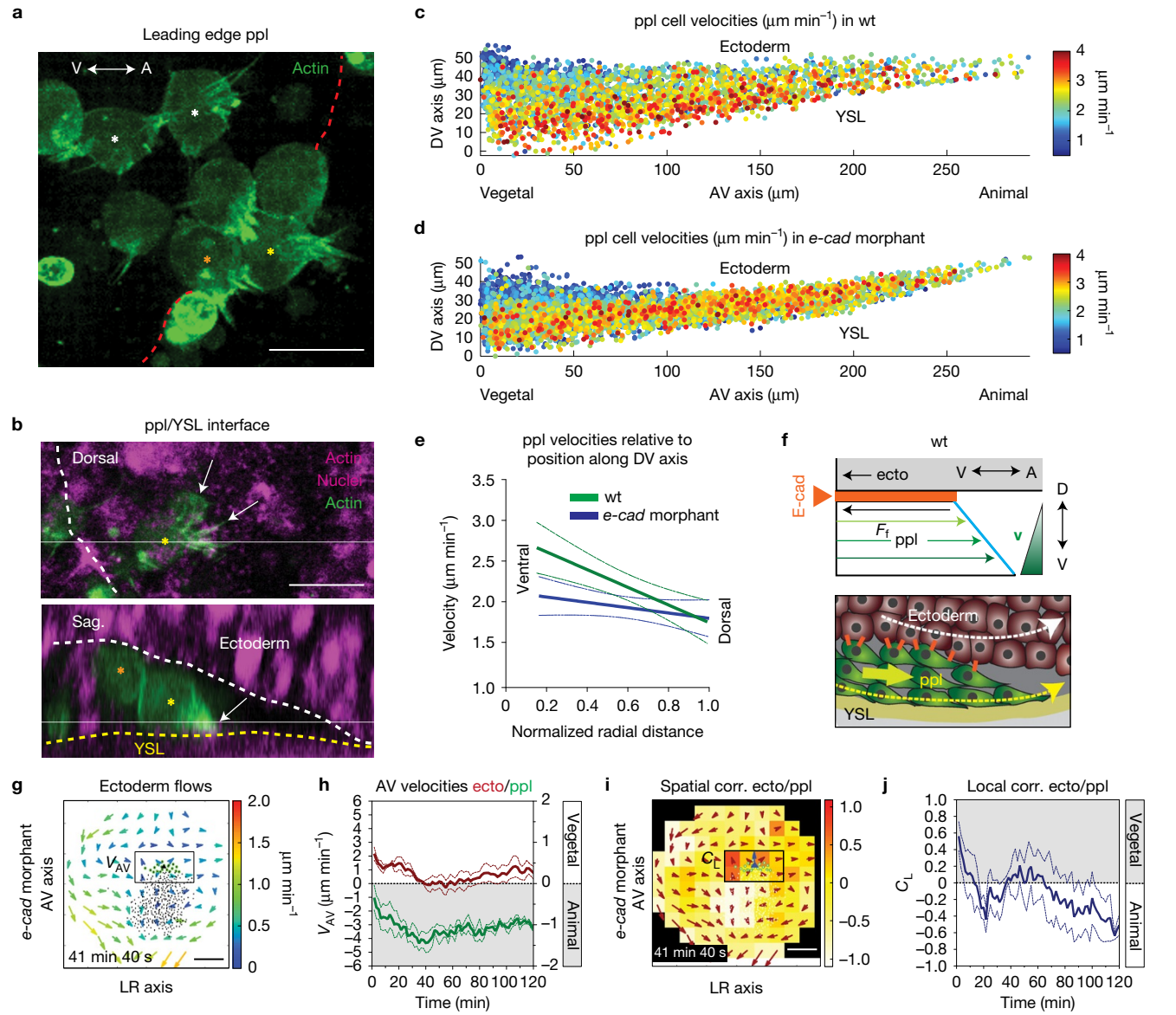

Figure 6 E-cadherin-mediated friction forces between ppl and ecto determine ecto morphogenesis. (**a**,**b**) Confocal images of ppl donor cells expressing lifeact-GFP (actin, green) transplanted into the ppl leading edge (outlined by dashed red line in **a**) of a host embryo labelled with Utrophin-Cherry (actin, purple) and H2A-mCherry (nuclei, purple); asterisks, ppl cells at YSL interface (yellow), between YSL and ecto (orange), and at ecto interface (white); dorsal view as maximal *z*-stack projection (**a**); dorsal (top) and sagittal (bottom) confocal sections with ppl protrusions (arrows) and interfaces to YSL (yellow dashed lines) and ecto (white dashed lines) indicated (**b**). (**c**,**d**) Average instantaneous velocities of migrating ppl cells in a wt (**c**) and *e-cadherin* morphant embryo (**d**) along the AV and DV axis colour-coded from 0 (blue) to 4 (red) μm min^{-1}. (**e**) Linear regression lines of binned mean velocities of ppl cells along the normalized radial distance of the DV axis from ventral (0) to dorsal (1) for wt (green; $P = 0.0006$, $n = 6$ embryos) and *e-cadherin* morphant embryos (blue; $P = 0.15$; $n = 4$ embryos); *P* values from *F*-test with null hypothesis; $P > 0.05$, slope equals zero; error bars (dashed lines), s.e.m. (**f**) Schematic illustrating ppl (yellow arrow) dragging ecto cells (white arrow) and friction forces slowing down ppl cells at the ppl/ecto interface (bottom), leading to a linear velocity gradient within ppl (top); F_f, friction force; E-cadherin, orange line/dots. (**g**) 2D tissue flow map indicating velocities of ecto cell movements along the AV (V_{AV}) and left–right (LR) (V_{LR}) axis at the dorsal side of an *e-cadherin* morphant embryo at 6.7 hpf; local average ecto velocities indicated and colour-coded from 0 (blue) to 2 (red) μm min^{-1}; positions of all/leading edge ppl cells, black/green dots; boxed area used for measurements in **h**. (**h**) Mean velocities along the AV axis (V_{AV}) of ecto (red; boxed area in **g**; right *y* axis) and underlying ppl leading edge cells (green, left *y* axis) in *e-cadherin* morphant embryos ($n = 4$ embryos); 6–8 hpf; error bars (dashed lines), s.e.m. (**i**) 3D directional correlation between leading edge ppl and adjacent ecto cells in an *e-cadherin* morphant embryo at 6.7 hpf; correlation colour-coded from 1 (red, highest) to −1 (white, lowest); red arrows, local averaged ecto velocities; boxed area used for measurements in **j**. (**j**) 3D directional correlation values between leading edge ppl and adjacent ecto cells (boxed area in **i**) in *e-cadherin* morphant ($n = 4$ embryos); 6–8 hpf; error bars (dashed lines), s.e.m. Scale bars, 20 μm (**a**,**b**) and 100 μm (**g**,**i**); arrows, AV and DV axes.

friction between these tissues. We therefore tested whether E-cadherin is needed to sustain coupling of ppl with neurectoderm cell movements by lowering the amount of E-cadherin expressed within the gastrulating embryo using *e-cadherin (cdh1)* morpholinos[22]. Consistent with previous reports[22–24], we found that in *e-cadherin* morphant embryos neurectoderm cell movements towards the vegetal pole were

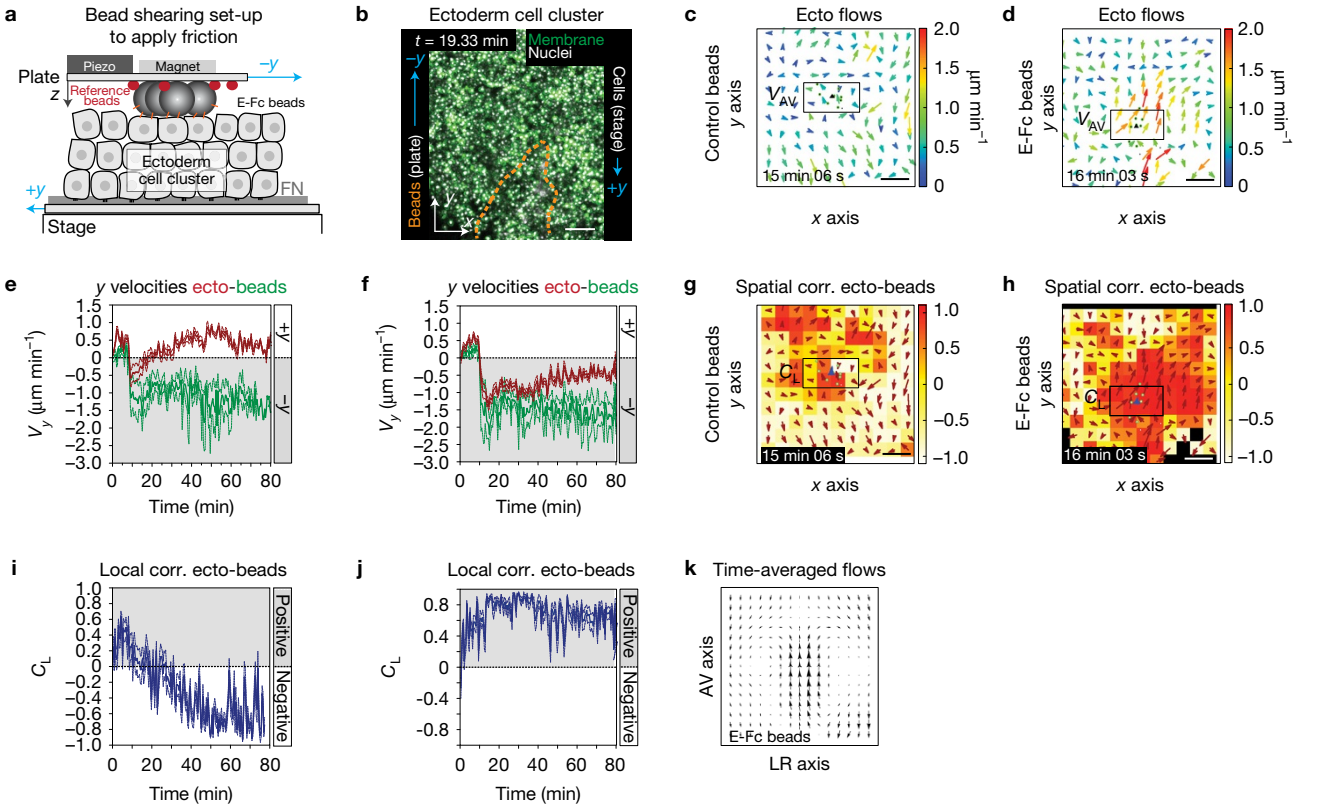

Figure 7 E-cadherin-mediated friction is sufficient to reorient ecto cell movements *in vitro*. (**a**) Illustration of parallel plate set-up for application of friction on ecto cells *in vitro*; uncoated control or coated with E-cadherin/Fc (E-Fc) polystyrene beads were sheared uniaxial ($-y$) over a cluster of opposing moving ecto cells ($+y$) to create friction; fluorescent reference beads (red) absorbed to the top plate were used to track the position and movement of adjacent polystyrene beads; E-cadherin receptors (orange) mediating friction are indicated. FN, fibronectin. (**b**) Maximum projection confocal image of ecto cell cluster expressing GPI-GFP (membrane, green) and H2A-mCherry (nuclei, white) plated onto a fibronectin-coated dish; directions of cell/stage movement ($+y$; velocity ~0.5 μm min^{-1}) and E-Fc-coated beads/top plate movement ($-y$; velocity ~1.5 μm min^{-1}) are indicated; position of cluster of beads above ecto cells is outlined (orange dashed line). (**c**,**d**) 2D tissue flow map indicating average velocities of ecto cell movements along the y (V_y) and x (V_x) axis after application of friction using control (**c**) or E-Fc-coated (**d**) beads at a representative time point; local average ecto velocities indicated and colour-coded ranging from 0 (blue) to 2 (red) μm min^{-1}; positions of leading edge polystyrene beads are marked by green dots; boxed area was used for measurements in **e**,**f**. (**e**,**f**) Mean velocities along the y axis (V_y) of leading edge control (**e**; $n=3$ experiments) or E-Fc-coated (**f**; $n=3$ experiments) beads (green) and adjacent ecto cells (boxed area in **c**,**d**; red curve) plotted before ($t=0$–10 min) and after ($t=10$–80 min) application of friction; error bars (dashed lines), s.e.m. (**g**,**h**) 3D directional correlation between ecto cells and adjacent control (**g**) or E-Fc-coated beads (**h**) at a representative time point; correlation colour-coded ranging from 1 (red, highest) to −1 (white, lowest); red arrows indicate local averaged ecto velocities; position of all/leading edge ppl cells marked by white/green dots; blue arrowhead indicates average velocity of ppl leading edge cells; boxed area was used for measurements in **i**,**j**. (**i**,**j**) 3D average directional correlation between ecto cells (boxed area in **g**,**h**) and leading edge control (**i**; $n=3$ experiments) or E-Fc-coated beads (**j**; $n=3$ experiments) before ($t=0$–10 min) and after ($t=10$–80 min) application of friction. (**k**) Time-averaged tissue flow map (over 70 (10–80) min from 3 experiments) of ecto cell movements along the y (V_y) and x (V_x) axis after application of friction using E-Fc-coated beads; error bars, s.e.m. Scale bars, 100 μm (**b**,**c**,**d**,**g**,**h**).

strongly reduced whereas the EVL/YSL advanced normally in the direction of the vegetal pole (Supplementary Fig. 7a,b). Additionally we observed that under reduced E-cadherin levels, ppl progenitor cells display less correlated movements towards the animal pole with slightly diminished velocity (Supplementary Fig. 7c–f). Notably, the influence of animal-directed ppl cell migration on the overlying adjacent neurectoderm cells was drastically diminished showing nearly exclusively vegetal-directed movements of neurectoderm cells (Fig. 6g,h and Supplementary Video 11). Consequently, the directional correlation between ppl and neurectoderm cell movements was nearly completely abolished ($C_{L(t120)} = -0.14 \pm 0.03$ (s.e.m., $n=4$ embryos); Fig. 6i,j and Supplementary Video 12), and the DV velocity gradient of cells within the ppl was much less pronounced (Fig. 6d,e and Supplementary Fig. 7g). This suggests that E-cadherin is critical for building up friction at the neurectoderm/ppl interface. Notably, the loss of correlation of directional movement between ppl and neurectoderm cells in *e-cadherin* morphant embryos was accompanied by a more vegetal positioning of the anterior neural anlage (Supplementary Fig. 7l,m), underlining the importance of coupling neurectoderm to ppl cell movement for positioning of the neural anlage.

E-cadherin has previously been suggested to be required for radial cell intercalations within the ectoderm and ectoderm epiboly movements[23,24]. To exclude that the observed loss of ppl and neurectoderm tissue coupling in *e-cadherin* morphant embryos is merely due to a failure of E-cadherin function within the ectoderm, we transplanted *e-cadherin* morphant ppl cells into MZ*oep* mutants that were beforehand injected with *CA-Mypt* messenger RNA into the YSL to increase the effect of ppl cells on adjacent neurectoderm

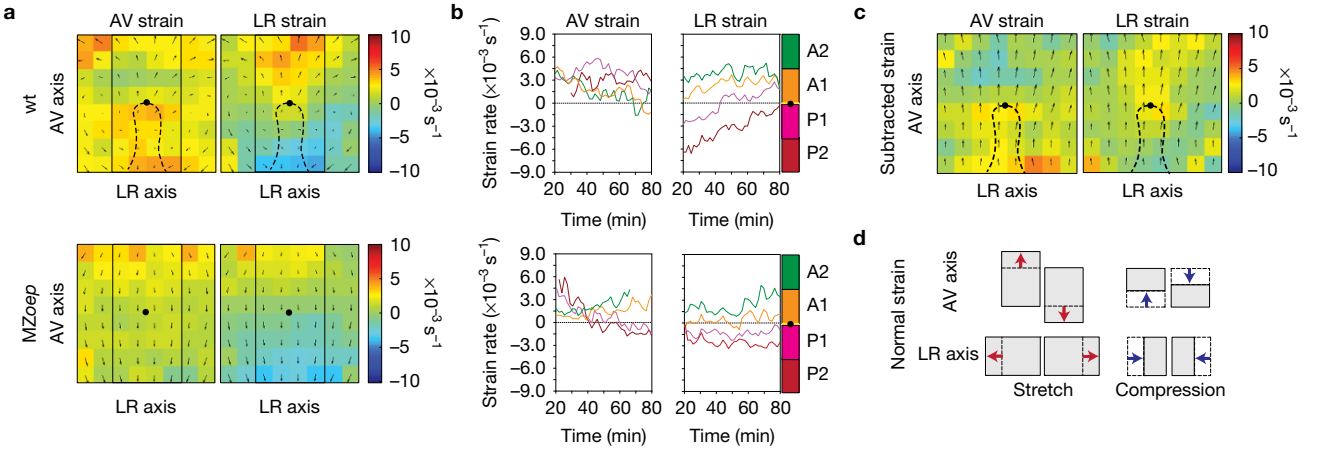

Figure 8 Friction forces trigger tissue deformations within the ecto. (**a**) Ecto tissue deformations along the AV and LR axes of wt (upper panels; $n=3$) and MZ*oep* (lower panels; $n=3$) embryos plotted as time-averaged strain values for each domain ($50\times50\,\mu m$); average normal strain rate is colour-coded according to amount of stretch (minimum green (0) to maximum red ($10\times10^{-3}\,s^{-1}$)) or compression (minimum green (0) to maximum blue ($-10\times10^{-3}\,s^{-1}$)); tissue flows of ecto are indicated as time-averaged velocities; the dashed line indicates ppl position and the black dot marks the ppl leading edge as reference point in wt and MZ*oep*; the rectangle outlines the area used for defining sectors along the AV axis in **b**. (**b**) Mean normal strain rates of ecto tissue along the AV (left panels) and LR (right panels) axes of wt (upper panels; $n=3$ embryos) and MZ*oep* (lower panels; $n=3$ embryos) embryos in defined sectors ($100\times200\,\mu m$) of the ecto (A1 and A2 anterior and P1 and P2 posterior of ppl leading edge; for a detailed description refer to Supplementary Fig. 1e) as a function of time during gastrulation (plotted from 6.3–7.3 in 10 min intervals); amount of stretch/compression within each sector is plotted along the *y* axis. (**c**) Ecto tissue strain rate maps derived by subtraction of AV (left panel) and LR (right panel) time-averaged strain values of wt from MZ*oep* mutant embryos ($n=3$ embryos); colour-coded as in **a**; tissue flows of ecto are indicated as time-averaged velocities; black dot marks ppl leading edge as reference point. (**d**) Illustration of kind and direction of tissue deformation in the ecto derived from normal strain; the arrows indicate the direction of stretch or compression of a tissue domain along the AV and LR axes dependent on the direction and magnitude of ecto movements.

cells as observed earlier (Fig. 4f–j). We found that animal-directed movements of *e-cadherin* morphant ppl cells were nearly unaltered compared to transplanted wt ppl cells (compare Supplementary Fig. 7i to Fig. 4h). However, the effect of morphant ppl cells on rearrangement of cell movements within the neurectoderm was significantly diminished and shorter-lived compared with their wt counterparts (Supplementary Fig. 7h,i), leading to an overall reduced alignment of movements between neurectoderm and ppl cells ($C_{L(t80)}=0.22\pm0.05$ (s.e.m., $n=4$ embryos); Supplementary Fig. 7j,k). Together, our analysis of *e-cadherin* morphant embryos and cells support a critical function for E-cadherin in generating friction between ppl and neurectoderm, which is essential for force transduction between those tissues and, consequently, positioning of the neural anlage.

E-cadherin-mediated friction between neurectoderm and ppl is sufficient to reorient neurectoderm cell movements

Vertical signalling from the axial mesendoderm to the overlying neurectoderm has been shown to be an important determinant of axial patterning within the forming neural keel[4,25] and thus could in principle contribute to the observed influence of ppl on neurectoderm movement. To address this possibility, we thought to test whether E-cadherin-mediated friction alone might be sufficient to explain the observed effect of ppl on neurectoderm movement in the embryo. Hence, we designed an *in vitro* experiment where we substituted ppl cells with a layer of E-cadherin -coated beads and sheared them over a cluster of *ex vivo* cultured ectoderm progenitor cells to create friction between them (Fig. 7a). To mimic similar conditions as in the embryo, we moved the labelled ectoderm cell cluster (GPI-GFP membrane and H2A-mCherry nuclei) in one direction (stage movement $\sim0.5\,\mu m\,min^{-1}$) and the E-cadherin -coated beads, mimicking the ppl, with higher velocities (top plate $\sim1.5\,\mu m\,min^{-1}$) in the opposite direction of the ectoderm cell cluster (Fig. 7a,b and Supplementary Fig. 8a–c). Remarkably, we observed that this movement of E-cadherin -coated beads was sufficient to reorient cell movements within the ectoderm cell cluster (Fig. 7d,f), leading to high local correlation between bead and ectoderm cell movements (Fig. 7h,j) and to generate double vortex flows within the ectoderm cluster reminiscent of the situation *in vivo* (Fig. 7k). In contrast, no such effects were obtained when using uncoated control beads (Fig. 7c,e,g,i), suggesting that E-cadherin-mediated contact between beads and ectoderm cells is critical for the beads to reorient ectoderm cell movements. Collectively, these findings support the view that E-cadherin-mediated friction between ppl and neurectoderm cells is sufficient to explain the observed effect of ppl on neurectoderm movement in the embryo.

Friction forces lead to distinct tissue deformations within the neurectoderm

To further corroborate the role of frictional forces on neurectoderm morphogenesis, we asked whether neurectoderm cells become compressed in front of the ppl cells and stretched behind, as one would expect if the ppl cells would be pushing the overlying neurectoderm towards the animal pole. To this end, we compared neurectoderm tissue deformation in wt versus MZ*oep* mutant embryos by calculating normal tissue domain strain rates along the AV and left–right (LR) axes (Fig. 8d; normal strain) and shear strain rates (Supplementary Fig. 8h) from measured neurectoderm cell velocities. We observed that both normal and shear strain rates appeared considerably different between wt and MZ*oep* mutant embryos during the course of

gastrulation (Fig. 8a,b and Supplementary Fig. 8e,f). In particular, when subtracting the time-averaged strain rates of MZ*oep* from wt embryos (Fig. 8c), we found a pronounced elongation of the neurectoderm along the AV axis behind the ppl leading edge, while ahead of the ppl the neurectoderm was compressed along the AV axis and elongated along the LR axis. Moreover, we found inverse shear deformations of the neurectoderm in areas left and right of the ppl in wt, but not in MZ*oep* mutant embryos (Supplementary Fig. 8e–g). Together, these distinct tissue deformations in wt compared with MZ*oep* mutant embryos are consistent with the notion that the ppl pushes the overlying neurectoderm towards the animal pole.

DISCUSSION

Biochemical signals from the axial mesendoderm have long been thought to trigger cell fate specification and patterning of the developing neural anlage[4,25]. Our finding that the generation of friction forces at the neurectoderm–mesendoderm interface is critical for proper positioning of the neural anlage during gastrulation shows that alongside biochemical, also mechanical signals play an important role for mesendoderm influencing neural plate development. Interestingly, the extent by which mesendoderm affects neurectoderm morphogenesis depends on the magnitude of friction force generated at the tissue interface, which again is determined by the speed difference between those tissues. This suggests that the regulation of differential speed between neurectoderm and mesendoderm during gastrulation constitutes an important factor determining neurectoderm morphogenesis.

Our data also suggest that friction forces at the neurectoderm/mesendoderm interface are generated by transient E-cadherin-mediated heterotypic contacts between ppl and neurectoderm cells. While the friction coefficient ($\sim$1 pN s μm^{-3}) at the neurectoderm/ppl interface estimated from our simulations is in principle compatible with this notion, directly confirming this by comparing an estimated with an expected friction coefficient due to E-cadherin-mediated transient interactions between ppl and neurectoderm cells remains difficult as long as number, lifetime and elasticity of E-cadherin bonds at the tissue interface are unknown. Still, our genetic and biophysical experiments, and in particular the E-cadherin loss-of-function approaches, strongly argue in favour of a decisive function of E-cadherin in friction generation at the neurectoderm/ppl interface.

Mechanical coupling between mesendoderm and neurectoderm, potentially mediated by ECM accumulation at the interface between these tissues, has previously been speculated to be required for coordination of their convergence movements during neurulation[7,8]. Yet, whether and how such potential mechanical coupling between these tissues might lead to the generation of forces at their interface, and how such forces are transmitted between the tissues is yet unclear. Furthermore, large vortex cell flows have previously been observed within the chicken epiblast during primitive streak formation[26,27]. Yet, given that these large-scale tissue flows occur before ingression of mesoderm and endoderm progenitors and are thought to be driven by cell shape changes and cell intercalations within the epiblast itself[28,29], the role of friction forces in this process remains uncertain.

Our observations that ppl mesoderm directly affects the movements of the neurectoderm through friction forces at their interface unravel an important yet unrecognized mechanical function of the mesendoderm in neurectoderm morphogenesis. Friction forces emerging at the interface between fluids and the plasma membrane have previously been implicated in vascular development[30] and tissue deformation during *Drosophila* gastrulation[31]. Our findings demonstrate that the generation of friction forces between forming tissues sliding against each other constitutes a key regulatory mechanism of embryo morphogenesis in development. □

METHODS

Methods, including statements of data availability and any associated accession codes and references, are available in the online version of this paper.

Note: Supplementary Information is available in the online version of the paper

ACKNOWLEDGEMENTS

We would like to thank R. Hauschild for technical assistance and the scientific service units at the IST Austria for continuous support. This work was supported by grants from the OMAA Ernst Mach Predoctoral Scholarship to Z.Á., Cancer Research UK to M.T., the Spanish Ministry of Economy and Competitiveness 'Centro de Excelencia Severo Ochoa 2013–2017' and CERCA Programme/Generalitat de Catalunya to V.R., the European Union's Seventh Framework Program/ERC Grant Agreement to B.H. (306589) and to T.V. (COLLMOT project; 227878), the Francis Crick Institute, which receives its core funding from Cancer Research UK (FC001317), the UK Medical Research Council (FC001317) and the Wellcome Trust (FC001317) to S.G. and G.S., and the Austrian Science Foundation (FWF): I930-B20 to C.-P.H.

AUTHOR CONTRIBUTIONS

M.S. and C.-P.H. conceived the project and designed the experiments; M.S. performed the experiments and data analysis with support from D.Č. for *in-situ* hybridizations and analysis, M.B. for *CA-Mypt* injections and EVL/YSL analysis and E.P. for immunohistochemistry.; Z.Á. developed computational tools for data analysis; S.S. and V.R. wrote scripts for data analysis; S.G. and G.S. developed the theory and S.G., S.S. and G.S. performed quantitative modelling; B.H. contributed to model interpretation; M.T. developed reagents and T.V. contributed to collective motion analysis and interpretation; M.S., G.S. and C.-P.H. wrote the paper.

COMPETING FINANCIAL INTERESTS

The authors declare no competing financial interests.

Published online at http://dx.doi.org/10.1038/ncb3492

1. Lecuit, T., Lenne, P.-F. & Munro, E. Force generation, transmission, and integration during cell and tissue morphogenesis. *Annu. Rev. Cell Dev. Biol.* **27,** 157–184 (2011).
2. Heisenberg, C.-P. & Bellaïche, Y. Forces in tissue morphogenesis and patterning. *Cell* **153,** 948–962 (2013).
3. Solnica-Krezel, L. & Sepich, D. S. Gastrulation: making and shaping germ layers. *Annu. Rev. Cell Dev. Biol.* **28,** 687–717 (2012).
4. Wilson, S. W. & Houart, C. Early steps in the development of the forebrain. *Dev. Cell* **6,** 167–181 (2004).
5. Appel, B. Zebrafish neural induction and patterning. *Dev. Dynam.* **219,** 155–168 (2000).
6. Woo, K. & Fraser, S. E. Order and coherence in the fate map of the zebrafish nervous system. *Development* **121,** 2595–2609 (1995).
7. Araya, C. *et al.* Mesoderm is required for coordinated cell movements within zebrafish neural plate *in vivo*. *Neural Dev.* **9,** 9 (2014).
8. Araya, C., Carmona-Fontaine, C. & Clarke, J. D. W. Extracellular matrix couples the convergence movements of mesoderm and neural plate during the early stages of neurulation. *Dev. Dynam.* **245,** 580–589 (2016).
9. Gritsman, K. *et al.* The EGF-CFC protein one-eyed pinhead is essential for nodal signaling. *Cell* **97,** 121–132 (1999).
10. Montero, J.-A. *et al.* Shield formation at the onset of zebrafish gastrulation. *Development* **132,** 1187–1198 (2005).
11. Latimer, A. & Jessen, J. R. Extracellular matrix assembly and organization during zebrafish gastrulation. *Matrix Biol.* **29,** 89–96 (2010).
12. Diz-Muñoz, A. *et al.* Control of directed cell migration *in vivo* by membrane-to-cortex attachment. *PLoS Biol.* **8,** e1000544 (2010).

13. Dumortier, J. G., Martin, S., Meyer, D., Rosa, F. M. & David, N. B. Collective mesendoderm migration relies on an intrinsic directionality signal transmitted through cell contacts. *Proc. Natl Acad. Sci. USA* **109,** 16945–16950 (2012).
14. Heisenberg, C. P. *et al*. Silberblick/Wnt11 mediates convergent extension movements during zebrafish gastrulation. *Nature* **405,** 76–81 (2000).
15. Ulrich, F. *et al*. Slb/Wnt11 controls hypoblast cell migration and morphogenesis at the onset of zebrafish gastrulation. *Development* **130,** 5375–5384 (2003).
16. Hatta, K., Kimmel, C. B., Ho, R. K. & Walker, C. The cyclops mutation blocks specification of the floor plate of the zebrafish central nervous system. *Nature* **350,** 339–341 (1991).
17. Thisse, C., Thisse, B., Halpern, M. E. & Postlethwait, J. H. Goosecoid expression in neurectoderm and mesendoderm is disrupted in zebrafish cyclops gastrulas. *Dev. Biol.* **164,** 420–429 (1994).
18. Behrndt, M. *et al*. Forces driving epithelial spreading in zebrafish gastrulation. *Science* **338,** 257–260 (2012).
19. Krieg, M. *et al*. Tensile forces govern germ-layer organization in zebrafish. *Nat. Cell Biol.* **10,** 429–436 (2008).
20. Weber, G. F., Bjerke, M. A. & DeSimone, D. W. A mechanoresponsive cadherin-keratin complex directs polarized protrusive behavior and collective cell migration. *Dev. Cell* **22,** 104–115 (2012).
21. Morita, H. *et al*. The physical basis of coordinated tissue spreading in zebrafish gastrulation. *Dev. Cell* **40,** 354–366.e4 (2017).
22. Babb, S. G. & Marrs, J. A. E-cadherin regulates cell movements and tissue formation in early zebrafish embryos. *Dev. Dynam.* **230,** 263–277 (2004).
23. Kane, D. A., McFarland, K. N. & Warga, R. M. Mutations in half baked/E-cadherin block cell behaviors that are necessary for teleost epiboly. *Development* **132,** 1105–1116 (2005).
24. Shimizu, T. *et al*. E-cadherin is required for gastrulation cell movements in zebrafish. *Mech. Dev.* **122,** 747–763 (2005).
25. Wessely, O. & De Robertis, E. M. Neural plate patterning by secreted signals. *Neuron* **33,** 489–491 (2002).
26. Cui, C., Yang, X., Chuai, M., Glazier, J. A. & Weijer, C. J. Analysis of tissue flow patterns during primitive streak formation in the chick embryo. *Dev. Biol.* **284,** 37–47 (2005).
27. Fleury, V. Clarifying tetrapod embryogenesis by a dorso-ventral analysis of the tissue flows during early stages of chicken development. *BioSystems* **109,** 460–474 (2012).
28. Rozbicki, E. *et al*. Myosin-II-mediated cell shape changes and cell intercalation contribute to primitive streak formation. *Nat. Cell Biol.* **17,** 397–408 (2015).
29. Voiculescu, O., Bodenstein, L., Lau, I.-J. & Stern, C. D. Local cell interactions and self-amplifying individual cell ingression drive amniote gastrulation. *eLife* **3,** e01817 (2014).
30. Tzima, E. *et al*. A mechanosensory complex that mediates the endothelial cell response to fluid shear stress. *Nature* **437,** 426–431 (2005).
31. He, B., Doubrovinski, K., Polyakov, O. & Wieschaus, E. Apical constriction drives tissue-scale hydrodynamic flow to mediate cell elongation. *Nature* **508,** 392–396 (2014).

DOI: 10.1038/ncb3492

METHODS

Embryo staging and fish line maintenance. Zebrafish (*Danio rerio*) were maintained as described previously[32]. Embryos were raised at 28–31 °C in E3 buffer and staged according to morphological criteria[33]. Zebrafish lines (female and male between the age of 0.5–2.5 yr) used for obtaining embryos: wild-type (wt) strains TL and AB and the following transgenic and mutant lines were used: *MZoep*$^{tz257/tz2579}$ (ref. 9), *Tg*(*dharma:eGFP*)[34], *MZoep;Tg*(*dharma:eGFP*), *Tg*(*gsc:GFP*)[35], *Tg*(*gsc:GFP-CAAX*), *Tg*(*actb2:Cherry-UtrCH*) and *Tg*(*actb1:lifeact-GFP*)[18]. No cell lines were used in this study. All animal experiments were carried out along the guidelines of the Ethics and Animal Welfare Committee (ETK) in Austria.

Microinjections of mRNA morpholino antisense oligonucleotides and dextran. Capped mRNA for injection was synthesized using the SP6 mMessage mMachineKit (Ambion). For ubiquitous mRNA overexpression, 100 pg *h2afva-mCherry*, 75 pg *h2afva-tagBFP*[36] and 100 pg membrane RFP (*mRFP*) mRNAs were injected into 1-cell-stage embryos. To generate mesoderm progenitors, one-cell-stage *Tg*(*gsc*:GFP), *Tg*(*gsc:GFP-CAAX*) or *Tg*(*actb2:lifeact-GFP*) embryos were injected with 100 pg *cyclops* (*cyc*) mRNA[37] and 2 ng *casanova* (*cas*) morpholino (MO; GeneTools) oligonucleotides[19]. To downregulate myosin-II activity specifically within the YSL, 50–75 pg of mRNA encoding for a constitutively active myosin-II phosphatase 1 (*CA-Mypt*) consisting of the N terminus (amino acids 1–300) of the human myosin phosphatase targeting subunit 1 lacking the inhibitory domain[38], together with 100 pg of *h2afva-mCherry* mRNA, was directly injected into the YSL of embryos between 512K and high stage (2.75–3.3 hpf)[39]. To interfere with prechordal plate (ppl) progenitor cell number, 0.5–1 ng of *cyc* MO (GeneTools) targeted against the ATG start codon of the *cyc* cDNA was injected into one-cell-stage embryos[40]. To reduce E-cadherin and Wnt11 expression levels, 3–4 ng *e-cadherin* MO (GeneTools)[22] or 6 ng of *wnt11* MO (Gene Tools)[41], both targeted against the ATG start codon of the respective cDNAs, was injected into one-cell-stage embryos. Interstitial fluid was labelled by injection of dextran Alexa Fluor 647 (10,000 MW; ThermoFisher Scientific) at high stage (3.3 hpf) into the extracellular space at the animal pole of the developing embryo.

Sample preparation for live cell imaging. Embryos were mounted in 0.5% low-melting-point (LMP) agarose (Invitrogen) into agarose moulds inside a Petri dish and covered with E3 medium with the dorsal side of the embryo facing upwards. For imaging of cell-division-inhibited embryos, aphidicolin and hydroxyurea were added into the 0.5% LMP agarose solution.

High-resolution multiphoton imaging. For *in vivo* fluorescence imaging, embryos were mounted at 60% epiboly (6 hpf) and subsequently imaged on an upright multiphoton microscope (TrimScope II, LaVision) equipped with a W Plan-Apochromat 20 × 1.0 NA dipping lens (Zeiss). GFP, mCherry/RFP, Dextra-647 and BFP fluorescence were imaged at 900 nm, 1,100 nm and 810 nm excitation wavelength, respectively, using a Ti-sapphire femtosecond laser system (Coherent Chameleon Ultra) combined with optical parametric oscillator (Coherent Chameleon Compact OPO) technology. Excitation intensity profiles were adjusted to tissue penetration depth and *Z*-sectioning for imaging was set between 2–4.8 µm. For long-term imaging, videos were acquired for 100–140 min with a frame rate between 95–166 s. All embryos were imaged with a temperature control unit set to 28.5 °C, and embryos were checked for normal development after imaging.

Confocal imaging. For whole-embryo confocal imaging, embryos were imaged using a Leica SP5 confocal microscope equipped with a Leica 25× 0.95 NA water-dipping lens. The temperature during imaging was kept constant at 28.5 °C using a temperature chamber. To analyse YSL ring advancement, consecutive *z*-stacks (up to 150 µm depth) of *Tg*(*actb2:Cherry-UtrCH*) embryos throughout the course of epiboly were recorded. YSL ring advancement was determined by PIV analysis on maximum *z*-projections of acquired time-lapse *z*-stacks using a custom-designed Matlab script[18].

For whole-mount imaging, embryos probed with anti-fibronectin antibody were imaged with a Zeiss LSM510 Meta confocal microscope, using a 40×/NA1.0 water-dipping lens. Live cell imaging of *in vitro* experiments was performed on a Leica SP5 confocal microscope equipped with a 20×/NA0.7 air objective. Embedded sections of E-cadherin -stained embryos were imaged with a Leica SP5 TCS microscope, using a 63×/NA1.4 oil immersion objective. Live cell imaging of *in vitro* experiments was performed on a Leica SP5 TCS microscope equipped with a 20×/NA0.7 air objective.

Transplantation assays. For cell transplantation experiments, donor and host embryos were kept in Danieaus's solution (58 mM NaCl, 0.7 mM KCl, 0.4 mM $MgSO_4$, 0.6 mM $Ca(NO_3)_2$ and 5 mM HEPES (pH 7.6)) after dechorionation. *Tg*(*gsc:GFP*) or *Tg*(*gsc:GFP-CAAX*) donor embryos injected with *cyc* mRNA and *cas* MO were checked at 30% epiboly (3 hpf) for GFP expression, indicative of mesoderm induction[19]. Single or groups of cells (100–200 cells) were then removed from the animal pole of those embryos using a glass transplantation needle (20 µm diameter) and transplanted below the neurectoderm cells at the dorsal side close to the margin of a MZ*oep* host embryo at 60% epiboly (6 hpf). For detecting the dorsal side of the host embryo, *MZoep;Tg*(*dharma:eGFP*) embryos were used expressing Dharma:EGFP at their dorsal side. Transplanted embryos were mounted for imaging as described above.

***In situ* hybridization assays.** Whole-mount *in situ* hybridizations were performed as described previously[10]. For *notail* (*ntl*) and *otx2 in situ* hybridizations, antisense RNA probes were synthesized from partial sequences of the respective cDNAs. Images were taken with a dissecting stereo-microscope (Olympus SZX 12) equipped with a QImaging Micropublisher 5.0 camera.

Bead shearing on ectoderm aggregates. Beads were prepared as follows: 10 µl of a 0.5% w/v solution of magnetic polystyrene particles (10 and 20 µm diameter; Spherotech) was incubated for 2 h at 4 °C in either 100 µl of 1 × PBS (Hank's balanced salt solution) for control beads, or 100 µl of recombinant mouse E-cadherin/Fc chimaera (E-Fc) in 1 × PBS (50 µg µl^{-1}) to prepare E-cadherin -coated beads. Beads were centrifuged at 3,000*g* for 15 min, washed with 1 × HBSS (Hank's balanced salt solution) containing 1.3 mM $CaCl_2$) buffer, again centrifuged and then re-suspended in 1 × HBSS. Beads with passively absorbed E-Fc were stored up to two weeks at 4 °C. To test E-Fc coupling efficiency, control and E-Fc-coupled beads were boiled in 4 × NuPAGE LDS sample buffer (Thermo Scientific), supernatants were loaded on a 4–15% protein gel and E-Fc was detected by western blot using a rat monoclonal E-cadherin antibody (DECMA-1, Santa Cruz). For shearing E-Fc-coated beads over the surface of ectoderm aggregates, we developed a parallel plate device, consisting of a glass plate controlled by two piezo elements for nanometre-precision movements in the *y* and *z* direction. The glass plate was assembled on top of a stage containing an inlet for a cell culture dish, which was mounted on a Leica SP5 TCS confocal microscope. Magnetic polystyrene beads were assembled into elongated clusters (∼100–200 beads mimicking the size and shape of the ppl *in vivo*) and held in position at the bottom of the glass plate by a fixed magnet on top of the glass plate. As reference points, small fluorescent beads (4 µm Tetraspeck Microspheres; Invitrogen) were absorbed to the glass plate to track the location and movement of the magnetic polystyrene particles. For preparing ectoderm cell aggregates, MZ*oep* mutant embryos, injected with *H2A-mCherry* (nuclei) and *GPI-GFP* (membrane) mRNA at 1-cell stage, were dissociated at 4–5 hpf in DMEM/F12 media mixture, and ectoderm cells were harvested and seeded in clusters on fibronectin-coated glass dishes. polystyrene particles were positioned on top of the ectoderm cell cluster with slight indentation. To mimic the movements of ppl and ectoderm cells *in vivo*, ectoderm cells were moved continuously in one direction (∼0.5 µm min^{-1}) and polystyrene particles were sheared over the ectoderm cells (∼1.5 µm min^{-1}) in the opposite direction, resulting in a comparable velocity ratio (1:3) as in wt embryos. Velocity profiles and correlations were obtained from nuclei and bead positions and calculated similar to measured flow profiles in the embryo.

Whole-mount immunohistochemistry and antibodies. For whole-mount immunohistochemistry, embryos were fixed for 2 h with 2% paraformaldehyde in 1 × PBS, washed twice after fixation with 50 mM glycine in 1 × PBS, 0.05% Triton-X, 0.05% Tween (PBSTT), and pre-blocked with 5% purified bovine serum albumin (BSA, Sigma-Aldrich, A9418) in PBSTT. For fibronectin immunohistochemistry, embryos were fixed at 60%, 80% and 90% epiboly and fibronectin was detected using a primary rabbit anti-fibronectin antibody (Sigma-Aldrich, F3648; 1:100 dilution). For E-cadherin immunohistochemistry, embryos were fixed at 75–80% epiboly and E-cadherin was detected using a primary rabbit antibody against zebrafish E-cadherin (antibody facility MPI-CBG; 1:200 dilution). Incubation with primary antibodies was performed overnight in PBSTT with 2% purified BSA at 4 °C. Embryos were consequently washed with PBSTT 4× for 30 min and incubated overnight with secondary antibody (Alexa 488-conjugated goat anti-rabbit, ThermoFisher Scientific, A-11008; 1:5,000 dilution) and rhodamine-phalloidin for F-actin staining (ThermoFisher Scientific, R415; 1:200 dilution). Embryos were washed 4× for 30 min with PBSTT and nuclei were stained with DAPI nuclei acid stain (ThermoFisher Scientific, D1306).

Preparation of histological sections. For tissue sectioning, pre-stained embryos were re-fixed in 2% PFA, embedded in increasing concentrations of OCT medium (Tissue-Tek O.C.T. Compound, Sakura Finetek; 0%–10%–30%–50%–70%–90% diluted in 30% sucrose/PBS), shock-frozen in 90% OCT solution on dry ice, and cryo-sectioned at a thickness of 20 µm before embedding in ProLong Gold antifade mountant (ThermoFisher Scientific, P36930).

Calculations of tissue strain rates. Strain rates were calculated within the neurectoderm close to the animal–vegetal axis in the wt and MZ*oep* mutant embryos.

To calculate tissue strain rates, the neurectoderm tissue was subdivided into small domains of 50 μm² boxes in *xy* (~50 cells per domain per time point) and the velocity of cells within each box was averaged to calculate its instantaneous average ensemble. The strain rates were then calculated similar to a previous approach[42], by using spatial derivatives of the velocities within the neighbouring boxes along the animal–vegetal (AV) and lateral (LR) axes of the embryo, considering the adjacent domains. To distinguish direction and kind of strain, we calculated normal strain rates along the AV, LR axes and shear strain rates. Normal strain rates determine the stretch (positive value) or compression (negative value) across the tissue domain along a specific direction (AV or LR) and shear strain rates capture the change of angle when the tissue deforms, whereby the angle of the domain (unit of the tissue) can shrink (positive value) or enlarge (negative value) during deformation. Strain rates were calculated as follows:

$$\varepsilon_{\mathrm{AV}} = \frac{\partial v}{\partial y}$$

$$\varepsilon_{\mathrm{LR}} = \frac{\partial u}{\partial x}$$

$$\varepsilon_{\mathrm{shear}} = \frac{\partial u}{\partial y} + \frac{\partial v}{\partial x}$$

where x and y are mathematical representations of the LR and AV axes, u and v are the velocities in these directions respectively and ε resembles strain rate.

Image and data processing for flow and correlation analysis. Images acquired from multiphoton live cell imaging were initially processed with ImSpector software (LaVision Bio Tec) to compile channels from imaging data, and the exported files were further processed using Imaris software (Bitplane) to visualize the recorded channels in three dimensions. Full data sets containing all of the channels from live cell imaging were used for identifying embryo landmarks needed to align all embryos in the same way for comparison of different experiments. Each imaged embryo was rotated and aligned along the AV axis at the dorsal side of the embryo using the *gsc*:GFP, or in the case of MZ*oep* mutant embryos, the *dharma*:EGFP signal as dorsal marker for correct embryo orientation. Ppl progenitor nuclei were extracted by surface masking of the *gsc*:GFP signal within prechordal plate progenitors. Neurectoderm cell nuclei were calculated from non-surface masked areas, and nuclei of remaining deep cells including paraxial mesoderm, endoderm and YSN were identified by their characteristic positions/movements and then manually subtracted. Nuclei positions of ppl progenitors and neurectoderm cells in *xyz*-dimensions were extracted for each time point and used for further quantitative analysis.

Cell tracking data containing nuclei positions over time were analysed with custom-made Perl scripts. From the 3D cell positions instantaneous velocity of a cell i at time t was calculated as follows:

$$\mathbf{v}_i(t) = \frac{r_i(t+\Delta t) - r_i(t)}{\Delta t}$$

where $\mathbf{v}_i(t)$ is the velocity vector of cell i at time t and $r_i(t)$ is the position of cell i at time t and Δt is the elapsed time between two consecutive 3D image sets in the time-lapse videos.

Analysis and visualization of ppl progenitor cell movements. In this section we delineate different analysis types that are based on methods generally used to quantify collective motion behaviour[43,44] to characterize collective cell migration.

To visualize how individual cell movements correlate with the average movement of the ppl cell collective, we calculated correlation values between the direction of movement of each individual cell and the average movement direction of the collective as follows:

$$C_i(t) = \hat{\mathbf{v}}_i(t) \cdot \overline{\hat{\mathbf{v}}_{\mathrm{group}}(t)}$$

where $\hat{\mathbf{v}}_i(t)$ is the normalized 3D velocity vector of cell i and

$$\overline{\hat{\mathbf{v}}_{\mathrm{group}}(t)} = \frac{1}{N(t)} \sum_{i=1}^{N} \hat{\mathbf{v}}_i(t)$$

is the average normalized 3D velocity vector of the group at time t and $N(t)$ is the number of ppl cells at time t. We calculated $C_i(t)$ for every time point for each cell. $C_i(t)$ can take values between 1 (if a cell movement is perfectly aligned with the average movement of the ppl collective) and −1 (if a cell is moving in the opposite direction of the collective). Correlation values of individual cells $C_i(t)$ are indicated in images for a representative time point by the colour of the velocity vectors (Supplementary Fig. 2b).

To quantify the alignment of cell movements, we defined the 'order parameter' as the absolute value of the averaged normalized velocity as follows[45]:

$$\varphi(t) = |\overline{\hat{\mathbf{v}}_{\mathrm{group}}(t)}| = \left| \frac{1}{N(t)} \sum_{i=1}^{N} \hat{\mathbf{v}}_i(t) \right|$$

where $\hat{\mathbf{v}}_i(t)$ is the normalized velocity of a cell and $N(t)$ is the total number of cells at time t. $\varphi(t)$ can take values between 0 (if cells move randomly, disordered movement) and 1 (if cells move uniformly in the same direction, highly ordered movement; Supplementary Fig. 2c).

Calculations and visualization of neurectoderm flows. To quantify and visualize neurectoderm cell motion without ppl progenitor cells, we calculated velocity flow maps in spatially defined areas of the embryo. Three-dimensional cell velocity vectors were averaged in 50 by 50 μm² sectors in *xy* planes and over the full *z* direction for every time point to create a grid covering the whole area of the visualized embryo. For visualization we plotted *xy* projections of the 3D velocity vectors for every time point and reconstructed a velocity flow map. Magnitude of the average velocity, namely

$$\left| \frac{1}{N} \sum_{i=1}^{N} \mathbf{v}_i(t) \right|$$

where N is the number of cells in a sector at time t, was calculated and is indicated by the colour of the arrow in each sector. The centre point of the grid was determined as the middle point of the imaged area.

To quantify and visualize neurectoderm cell motion with underlying ppl progenitor cells, we determined the centre 0,0 point of the above-mentioned grid as the average position of the first 20 leading cells. We used this 0,0 grid position as a reference point to compare the cell movements from different embryos. For each time point of image acquisition, the 0,0 grid position was superimposed to keep the reference point fixed for every time frame and the 50 × 50 μm² sectors, containing the average instantaneous cell velocities, were back projected around this reference point (Fig. 2c and Supplementary Fig. 2e,f). This method allowed us to quantify cell velocities in the adjacent neurectoderm in a relative position to the leading ppl progenitor cells and to directly compare different data sets with each other.

Averaged neurectoderm velocity fields were calculated by making both time and ensemble averages for each experimental case. Time averages were taken over the whole duration of image acquisition (typically 120 min) for wt, *cyc* morphant, *slb* morphant, CA-Mypt and MZ*oep* mutant embryos and visualized as time-averaged neurectoderm flow velocity fields (Fig. 2g).

Directional correlation analysis of neurectoderm and prechordal plate progenitor cell movements. To quantify the correlation between the movement of neurectoderm ('ecto' in equations) and underlying ppl progenitor cells ('pp' in equations), we calculated their directional correlation in every sector of the grid (grids were positioned the same way as described above) for each time point as follows:

$$C_{\mathrm{ecto-pp}}(t) = \overline{\hat{\mathbf{v}}_{\mathrm{ecto}}(t)} \cdot \overline{\hat{\mathbf{v}}_{\mathrm{pp}}(t)}$$

where $\overline{\hat{\mathbf{v}}_{\mathrm{ecto}}(t)}$ and $\overline{\hat{\mathbf{v}}_{\mathrm{pp}}(t)}$ are the normalized averaged 3D velocity vectors in a grid at time t of neurectoderm and ppl progenitor cells, respectively (Supplementary Fig. 2g). $C_{\mathrm{ecto-pp}}(t)$ can take values between 1 (ectoderm and ppl progenitor cells move in the same direction) and −1 (they move in opposite directions). The $C_{\mathrm{ecto-pp}}(t)$ value of each grid sector is indicated in images and videos by the colour of the sector (Fig. 2e and Supplementary Fig. 2g,h).

To investigate the effect of ppl movement on neurectoderm cells that are positioned anterior to the leading edge of the ppl, we calculated the directional correlation between $\overline{\hat{\mathbf{v}}_{\mathrm{ecto}}(t)}$ and the average normalized velocity vector of the first 20 leading ppl cells as follows:

$$C_{\mathrm{ecto\text{-}leading}}(t) = \overline{\hat{\mathbf{v}}_{\mathrm{ecto}}(t)} \cdot \overline{\hat{\mathbf{v}}_{\mathrm{leading}}(t)}$$

The $C_{\mathrm{ecto\text{-}leading}}(t)$ value of each grid sector is indicated in images and videos by the colour of the sector (Fig. 1k).

Instantaneous speed, directionality and polarity analyses of ppl cells. Cell speed v_{Cell} was calculated from single cell trajectories with positions

$$\mathbf{r}(t) = (x(t), y(t), z(t))$$

DOI: 10.1038/ncb3492

Data were selected every frame to obtain instantaneous velocities

$$v = |\delta \mathbf{r}(n \cdot tlag)|/(n \cdot tlag)$$

with

$$\delta \mathbf{r}(n \cdot tlag) = \mathbf{r}(t + n \cdot tlag) - \mathbf{r}(t)$$

and *tlag* being the time interval between successive frames. Instantaneous velocity values v calculated from single trajectories were averaged to obtain the cell speed v_{Cell} (Supplementary Fig. 2d).

To calculate directionality values, single cell trajectories were split into segments of equal length (5 frames). Directionality indices for single trajectories were calculated via a sliding window as the ratio of start-to-end distance versus the summed distance between successive frames in a segment. Obtained directionality values were averaged over all segments in a single trajectory. This analysis yielded values between [0,1], with higher movement directionality closer to 1 (Supplementary Fig. 2d).

For the calculation of speed gradients along the DV axis bright-field images of embryos were obtained to measure the embryo radius R_E. The value R_E was used as an input parameter to fit (x, y, z) coordinates of ppl cells to a sphere with radius R_E to obtain the centre of the embryo (x_0, y_0, z_0). Ppl cell coordinates were shifted to the origin by linear translation

$$(x' = x - x_0, y' = y - y_0, z' = z - z_0)$$

and transformed to spherical coordinates $(x', y', z') \rightarrow (R, \theta, \varphi)$. In this reference frame the DV axis is represented by the R coordinate (the AP axis and LR axis by θ and φ coordinates respectively). Two-dimensional velocity maps along the DV and AV axis were generated from instantaneous velocity values $v(R, \theta)$ calculated as described above and plotted at interpolated cell positions between consecutive frames (Fig. 6c,d). Speed gradients along the DV axis were obtained from instantaneous velocities $v(R)$ and were binned and averaged to calculate mean instantaneous velocity values (Fig. 6e).

Direction of protrusion formation of transplanted ppl progenitor cells was analysed for each video in steps of 15–20 min with Fiji software using the angle measurement tool. Angle between detected protrusion and the AV axis was measured, where an angle of 0° corresponds to the animal and an angle of 180° to the vegetal pole, and a 90 and 270° angle for the right and left axis respectively. Angles were plotted in polar plots using IgorPro software (WaveMetrics) (Supplementary Fig. 5d).

Quantification of neural plate positioning. After whole-mount *in situ* hybridization, the embryos were imaged using a dissecting stereoscope with the Leica Imaging Application. Fiji software was utilized to fit a circle around the embryo and to measure the angle between the vegetal pole and the anterior border of the *otx2* expression domain by using the built-in angle tool. Box–whisker plots were generated to compare angles from different developmental stages (Supplementary Fig. 2m).

Statistical analysis and reproducibility. Statistical analysis was performed using software Prism 5 (GraphPad) and R (Bell Laboratories). To compare the mean values, unpaired Student's t-tests were used to calculate two-tailed P values for two-group comparison and Student's t-tests with Benjamini–Hochberg correction for multiple-group testing correction were used to calculate the false discovery rate for each P value. The data meet the assumption of the tests and the variance is estimated to be similar between groups that are compared. We used a non-parametric unpaired test because we assume that the data follow a Gaussian distribution and that in the compared groups the individual values were not paired or matched with one another. All P values are reported within the figure legends. All n-values report biological replicates (embryos) if not stated otherwise. No statistical method was used to predetermine the sample size. The experiments were not randomized. The investigators were not blinded to allocation during experiments and outcome assessment. For interpreting linear regression slopes we performed an F-test to report the P value (two-tailed) testing the null hypothesis that the overall slope is zero ($P > 0.05$). Where whisker–box plots were used, the centre of the box shows the median (the additional red dot shows the mean), and the whiskers show the minimum and maximum measured value, respectively (capped by 1.5 interquartile range; values measured outside are shown as outliers). Representative stereoscope/confocal/multiphoton images of zebrafish embryos, or *ex vivo* isolated cells, or western blot in Figs 1a,c,f, 2a,b,i,j, 3a,g,m,s, 6a,b and 7b and Supplementary Figs 1a–e, 2a,i,k,l, 3a,e,i,j, 4b,d,i, 5b–d,i,j, 7a,b,l and 8a–c have been successfully repeated between 3 and 6 times.

Code availability. Relevant computational codes used for data processing are available from the authors on request.

Data availability. All data that support the conclusions in the study are available from the authors on reasonable request.

32. Westerfield, M. *The Zebrafish Book. A Guide for the Laboratory Use of Zebrafish (Danio Rerio)* 4th edn (Univ. Oregon Press, 2000).
33. Kimmel, C. B., Ballard, W. W., Kimmel, S. R., Ullmann, B. & Schilling, T. F. Stages of embryonic development of the zebrafish. *Dev. Dynam.* **203,** 253–310 (1995).
34. Ryu, S. L. *et al.* Regulation of dharma/bozozok by the Wnt pathway. *Dev. Biol.* **231,** 397–409 (2001).
35. Doitsidou, M. *et al.* Guidance of primordial germ cell migration by the chemokine SDF-1. *Cell* **111,** 647–659 (2002).
36. Compagnon, J. *et al.* The notochord breaks bilateral symmetry by controlling cell shapes in the zebrafish laterality organ. *Dev. Cell* **31,** 774–783 (2014).
37. Rebagliati, M. R., Toyama, R., Haffter, P. & Dawid, I. B. cyclops encodes a nodal-related factor involved in midline signaling. *Proc. Natl Acad. Sci. USA* **95,** 9932–9937 (1998).
38. Weiser, D. C., Row, R. H. & Kimelman, D. Rho-regulated myosin phosphatase establishes the level of protrusive activity required for cell movements during zebrafish gastrulation. *Development* **136,** 2375–2384 (2009).
39. D'Amico, L. A. & Cooper, M. S. Morphogenetic domains in the yolk syncytial layer of axiating zebrafish embryos. *Dev. Dynam.* **222,** 611–624 (2001).
40. Karlen, S. & Rebagliati, M. A morpholino phenocopy of the cyclops mutation. *Genesis* **30,** 126–128 (2001).
41. Lele, Z., Bakkers, J. & Hammerschmidt, M. Morpholino phenocopies of the swirl, snailhouse, somitabun, minifin, silberblick, and pipetail mutations. *Genesis* **30,** 190–194 (2001).
42. Blanchard, G. B. *et al.* Tissue tectonics: morphogenetic strain rates, cell shape change and intercalation. *Nat. Methods* **6,** 458–464 (2009).
43. Vicsek, T. & Zafeiris, A. Collective motion. *Phys. Rep.* **517,** 71–140 (2012).
44. Méhes, E. & Vicsek, T. Collective motion of cells: from experiments to models. *Integr. Biol.* **6,** 831–854 (2014).
45. Szabó, B. *et al.* Phase transition in the collective migration of tissue cells: experiment and model. *Phys. Rev. E. Stat. Nonlin. Soft. Matter Phys.* **74,** 061908 (2006).

nature cell biology

DOI: 10.1038/ncb3492

In the format provided by the authors and unedited.

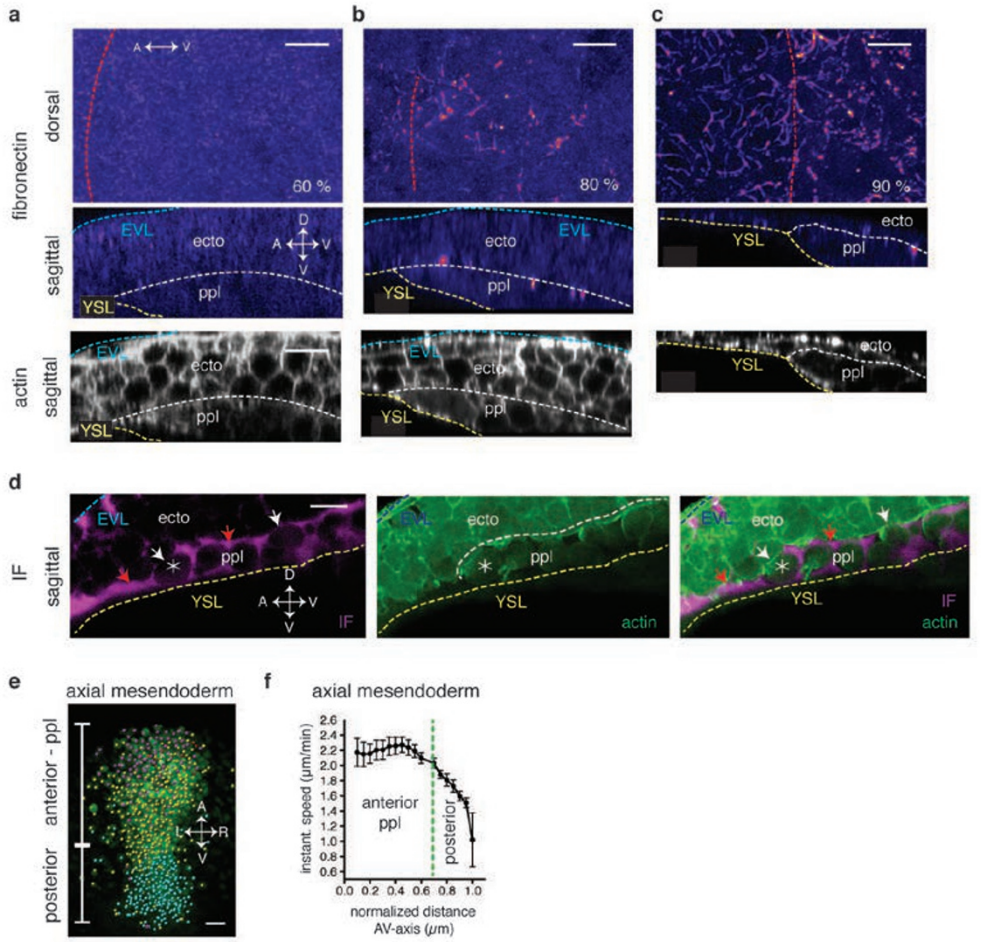

Supplementary Figure 1 Fibronectin and interstitial fluid localization at the neurectoderm-to-prechordal plate interface during zebrafish gastrulation. (a, b, c) Immunofluorescence confocal images of the neurectoderm (ecto)-to-prechordal plate (ppl) interface (white dashed line) in a wild type (wt) embryos at 6 (a), 8 (b), and 9 (c) hpf showing Fibronectin staining (pseudo-colored with Fire LUT) in maximum intens ity projections of dorsal views (top panels) and sagittal sections (middle panels); red dashed line outlines position of ppl leading edge cells; blue dashed line indicates ecto-to-EVL interface, and yellow dashed line shows YSL interface to ppl and ecto; bottom panels are sagittal sections of the ecto-to-ppl interface stained for F-actin (phalloidin) to mark this interface; double-sided arrows indicate animal (A) to vegetal (V) and dorsal (V) to ventral (V) embryo axes; asterisk labels ppl leading edge cell; scale bar, 20 µm. (d) Multiphoton live cell images showing interstitial fluid (IF) accumulation (dextran-Alexa Fluor 647, left panel), F-actin localization (*Tg*(*actb1:lifeact*-GFP), middle panel) and a combination of those different labels (right panel) at the ecto-to-ppl interface (white dashed line) at 7 hpf; red arrows indicate extracellular cavities filled with IF at the ecto-to-ppl and ecto-to-YSL interfaces; white arrows indicate ecto-to-ppl cell-cell contacts devoid of IF accumulations; blue dashed line indicates ecto-to-EVL interface, and yellow dashed line shows YSL interface to ppl and ecto; double-sided arrows indicate AV and dorsal DV embryo axes; asterisk labels ppl leading edge cell; scale bar, 20 µm. (e) Multiphoton live cell image of *Tg(gsc*:GFP) embryo (t = 120 min, 8 hpf) with pseudo-colored spots marking positions of nuclei within the axial mesendoderm (green); dorsal view with double-sided arrows indicating AP to VP and left (L) to right (R) embryo axes; color-code indicates mean total cell speeds of axial mesendoderm cells moving to the animal pole after internalization (cyan, 0-2 and yellow/magenta >2 µm/min); position of anterior (ppl) and posterior mesendoderm marked; scale bar, 50 µm. (f) Average instantaneous cell speeds in µm/min of internalized axial mesendoderm cells in wt embryos (n=6 embryos) plotted along the normalized distance along the AV axis from anterior (0) to posterior (1); green dashed line marks position of transition from anterior (ppl) to posterior axial mesendoderm, error bars, s.e.m.

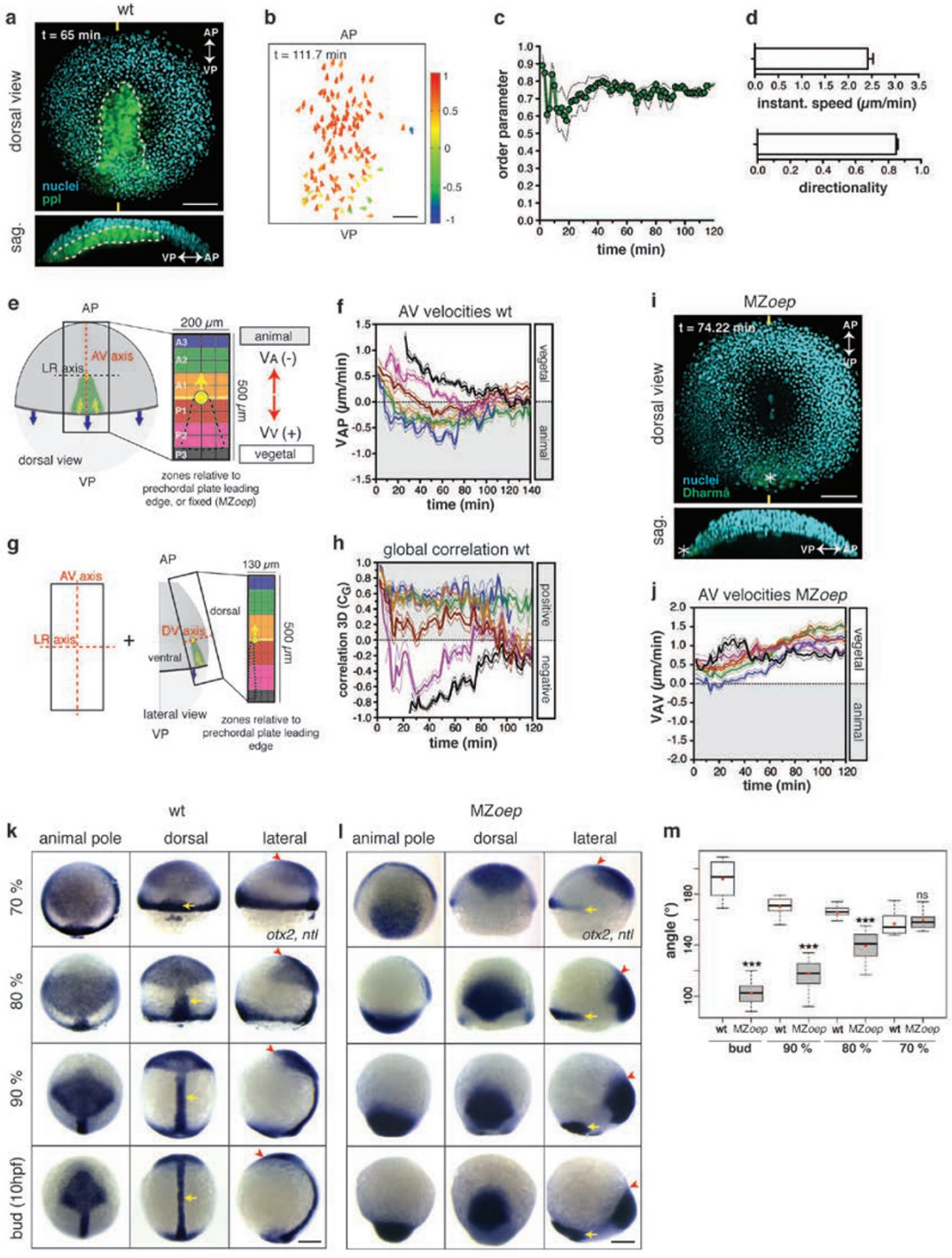

Supplementary Figure 2

Supplementary Figure 2 Prechordal plate and neurectoderm cell movements and neural plate positioning in wild type and MZ*oep* mutant embryos. (a) Fluorescent images of a wild type (wt) *Tg(gsc*:GFP) embryo showing neurectoderm nuclei (H2A-BFP, cyan) and *gsc*-expressing GFP-labeled prechordal plate (ppl) cells at a representative time point during gastrulation (t = 65 min, 7.1 hpf); dorsal and sagittal (dorsal up) sections through the embryo (yellow tags in upper panel mark sagittal section plane in lower panel); animal (AP) and vegetal pole (VP) indicated by arrows; scale bar, 100 µm. (b) Correlation of ppl cell movements in a wt embryo at a representative time point during gastrulation (t = 111.7 min, 7.9 hpf); ppl cells are visualized as arrows in a 2D plot and color-coded corresponding to their 3D correlation values between 1 (red, maximum correlation) and -1 (blue, minimum correlation); every 3rd cell is plotted; AP, animal pole; VP, vegetal pole; scale bar, 50 µm. (c) Average degree of alignment of ppl cell movements in wt embryos (n=5 embryos) plotted from 6 to 8 hpf (120 min); the order parameter corresponds to the degree of alignment ranging from 0 (disordered movement) to 1 (highly ordered movement); error bars, s.e.m. (d) Mean instantaneous cell speed and directionality of ppl cells in a wt embryo (n=5 embryos) calculated from 6 to 8 hpf are plotted as bar graphs; error bars, s.e.m. (e) Schematic illustration of global neurectoderm velocity measurements at the dorsal side of the embryo; the neurectoderm was segmented into 100 x 200 µm sectors along the AV axis (V_{AV}); sectors were positioned and color-coded relative to the ppl leading edge (yellow dot), or fixed for cases without ppl cells; A1-3 and P1-3, sector anterior and posterior of the ppl leading edge, respectively; mean V_{AV} velocities in the different sectors were calculated for each time frame. (f) Mean movement velocities (µm/min) along the AV axis (V_{AV}) of neurectoderm cells in wt embryos (n=6 embryos) plotted from 6 to 8 hpf (120 min); colors of curves correspond to respective sectors in (e); error bars, s.e.m. (g) Schematic illustration of global 3D movement correlation analysis between neurectoderm and ppl cells in defined sectors along the AV axis of the embryo. For 3D correlation calculations, neurectoderm cell velocities along the AV (V_{AV}), left-right (LR) (V_{LR}; see (e)) and dorsal-ventral (DV) axis (V_{DV} in sectors of 130x100 µm) were measured; sectors were positioned and color-coded relative to the ppl leading edge (yellow dot); A1-3 and P1-3, sector anterior and posterior of the ppl leading edge (yellow dot), respectively. (h) 3D movement correlation between leading edge ppl and adjacent neurectoderm cells in defined sectors along the AV axis of wt embryos (n=6 embryos) plotted from 6 to 8 hpf (120 min); colors of curves correspond to respective sectors in (e) and (g); error bars, s.e.m. (i) Fluorescent images of a MZ*oep;Tg(dharma:*EGFP*)* mutant embryo showing neurectoderm nuclei (H2A-BFP, cyan) and Dharma (*dharma:*EGFP, green, marked with asterisk) expression at the dorsal blastoderm margin at a representative time point during gastrulation (t = 74.22 min, 7.2 hpf); dorsal and sagittal (dorsal up) sections through the embryo (yellow tags in upper panel mark sagittal section plane in lower panel); animal (AP) and vegetal pole (VP) indicated by arrows; scale bar, 100 µm. (j) Mean movement velocities (µm/min) of neurectoderm cells along the AV axis (V_{AV}) in MZ*oep* mutant embryos (n=4 embryos) plotted over from 6 to 8 hpf (120 min); colors of curves correspond to sectors outlined in (e); error bars, s.e.m. (k, l) Anterior neural anlage in wt (k) and MZ*oep* mutant (l) embryos marked by whole-mount *in situ* hybridization of *otx2* mRNA expression at consecutive stages of gastrulation from 70% epiboly to bud stage (7 - 10hpf); posterior axial mesoderm was detected by *no tail (ntl)* mRNA expression (arrows); animal pole (dorsal down), dorsal (animal pole up) and lateral (dorsal right) views are shown; arrowheads mark the anterior most edge of the neural plate; scale bars 200 µm. (m) Quantitative analysis of neural plate position during gastrulation in MZ*oep* versus wt embryos. The angle (°) between the vegetal pole and the anterior border of the *otx2* expression domain was measured for embryos at different stages during gastrulation (k, l) and plotted as box-whisker graphs; n, embryos analyzed from 4 independent experiments; student's t-test (*P* value indicated) for all graphs comparing same stages; ***, $P<0.001$, (ns) non significant, $P>0.05$; n (wt, bud) = 36, n (wt, 90%) = 36, n (wt, 80%) = 34, n (wt, 70%) = 29, n (MZ*oep*, bud; $P<0.0001$) = 24, n (MZ*oep*, 90%; $P<0.0001$) = 36, n (MZ*oep*, 80%; $P<0.0001$) = 20, n (MZ*oep*, 70%; $P<0.358$) = 18; box plot centre, median; red dot, mean; upper whisker, maximum; lower whisker, minimum.

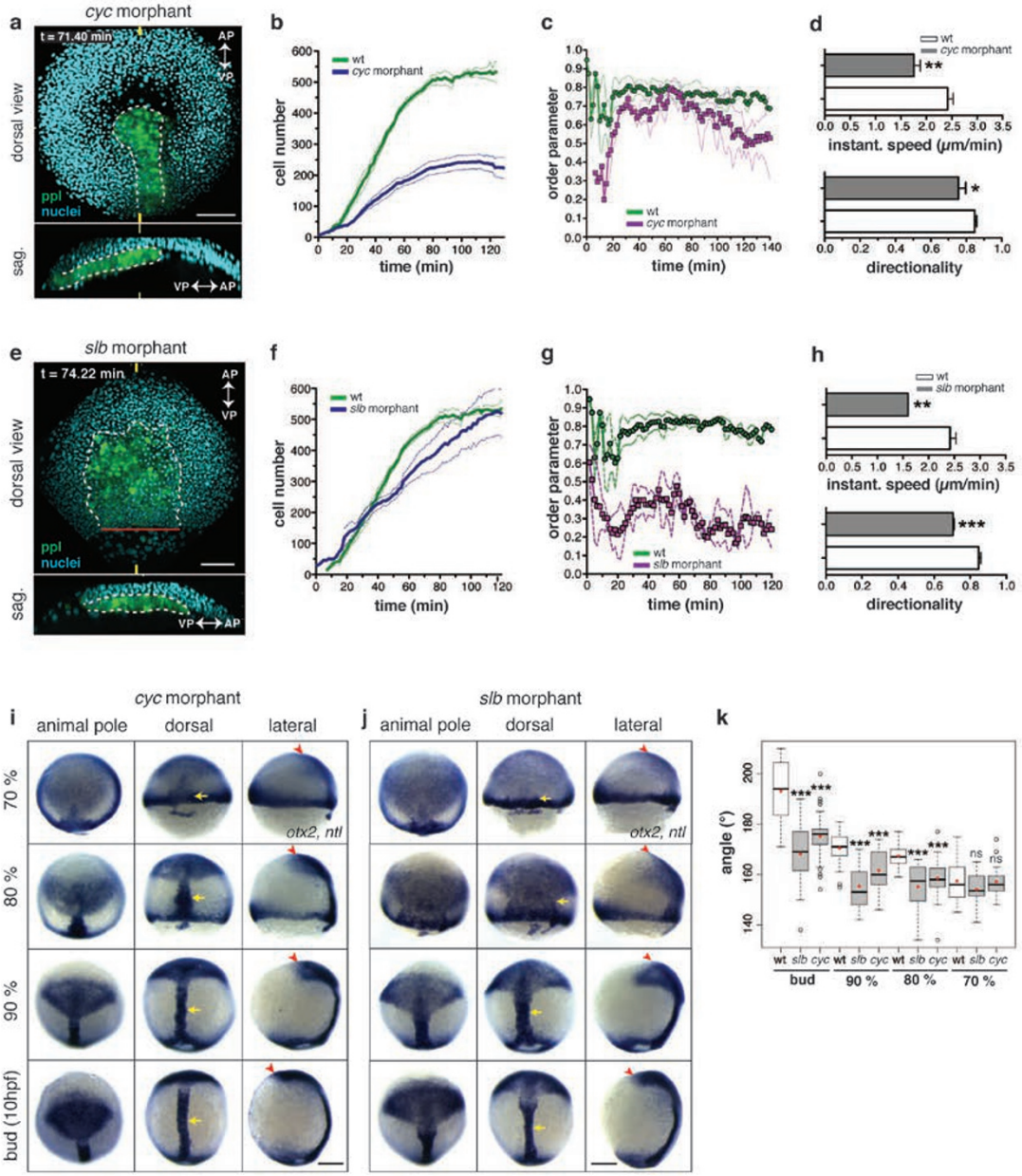

Supplementary Figure 3 Prechordal plate cell movements and neural plate positioning in *cyc* and *slb* morphant embryos. (a, e) Fluorescence images of a Tg(*gsc:*GFP) *cyclops (cyc)* (a) and *silberblick (slb)* morphant (e) embryo showing H2A-BFP expression (cyan) in all nuclei and GFP (green, white outline) expression in *gsc*-expressing prechordal plate (ppl) cells at a representative time point during gastrulation (a; t = 71.40 min, 7.2 hpf and e; t = 74.22 min, 7.2 hpf); dorsal and sagittal (dorsal up) sections through the embryo (yellow tags in upper panel mark sagittal section plane in lower panel); animal (AP) and vegetal pole (VP) indicated by arrows; red line in (e) indicates widened ppl internalization zone; scale bar, 100μm. (b, f) Number of internalized ppl cells in *Tg(gsc:*GFP) *cyc* (b; blue curve, n = 3 embryos) and *slb* (f; blue curve, n = 3 embryos) morphant embryos (blue curve, n = 3 embryos) versus wt (green curve, n = 6 embryos) embryos plotted between 6 and 8 hpf (120 min); error bars, s.e.m. (c, g) Average degree of alignment of ppl cell movements in *cyc* (c) magenta curve/squares, n = 3 embryos) and *slb* morphant (g; magenta curve/dots, n=3 embryos) versus wt (green curve/dots, see Supplementary Fig. 2c) embryos plotted from 6 to 8/8.3 hpf (120/140 min); the order parameter corresponds to the degree of alignment ranging from 0 (disordered movement) to 1 (highly ordered movement); error bars, s.e.m. (d, h) Mean instantaneous ppl cell speed and directionality of *cyc* [d; gray bar graph, n = 4 embryos; *P(speed)* = 0.0061, *P(dir)* = 0.033] and *slb* morphant [gray bar graphs, n = 3 embryos, *P(speed)* = 0.0025, *P(dir)* <0.0001] versus wt (white bar graph, see Supplementary Fig. 2d) embryos plotted as bar graphs; error bars, s.e.m.; student's t-test for all graphs; ***, p < 0.001, **, p < 0.01; *, p < 0.05. (i, j) Anterior neural plate anlage in *cyc* and *slb* morphant embryos marked by whole-mount in situ hybridization of *otx2* mRNA expression at consecutive stages of gastrulation from 70% epiboly to bud stage (7 - 10hpf); posterior axial mesoderm was detected by *no tail (ntl)* mRNA expression (arrows); animal pole (dorsal down), dorsal (animal pole up) and lateral (dorsal right) views are shown; arrowheads mark the most anterior edge of the neural plate; scale bar 200 μm. (k) Quantitative analysis of neural plate position in *cyc* and *slb* morphant versus wt embryos during gastrulation. The angle (°) between the vegetal pole and the anterior border of the *otx2* expression domain was measured for embryos at different stages during gastrulation (i, j) and plotted as box-whisker graphs; n, embryos analyzed from 4 independent experiments; student's t-test (*P* value indicated) for all graphs comparing same stages; ***, *P* <0.001, ns (non significant), *P* >0.05; n (wt, bud) = 36, n (wt, 90%) = 36, n (wt, 80%) = 34, n (wt, 70%) = 29, n (*slb*, bud; *P* <0.0001) = 23, n (*slb*, 90%; *P* <0.0001) = 17, n (*slb*, 80%; *P* <0.0001) = 20, n (*slb*, 70%; *P* = 0.134) = 16, n (*cyc*, bud; *P* <0.0001) = 40, n (*cyc*, 90%; *P* <0.0001) = 39, n (*cyc*, 80%; *P* <0.0001) = 32, n (*cyc*, 70%; *P* = 0.851) = 27; red dots mark mean values; box plot centre, median; red dot, mean; upper whisker, maximum; lower whisker, minimum.

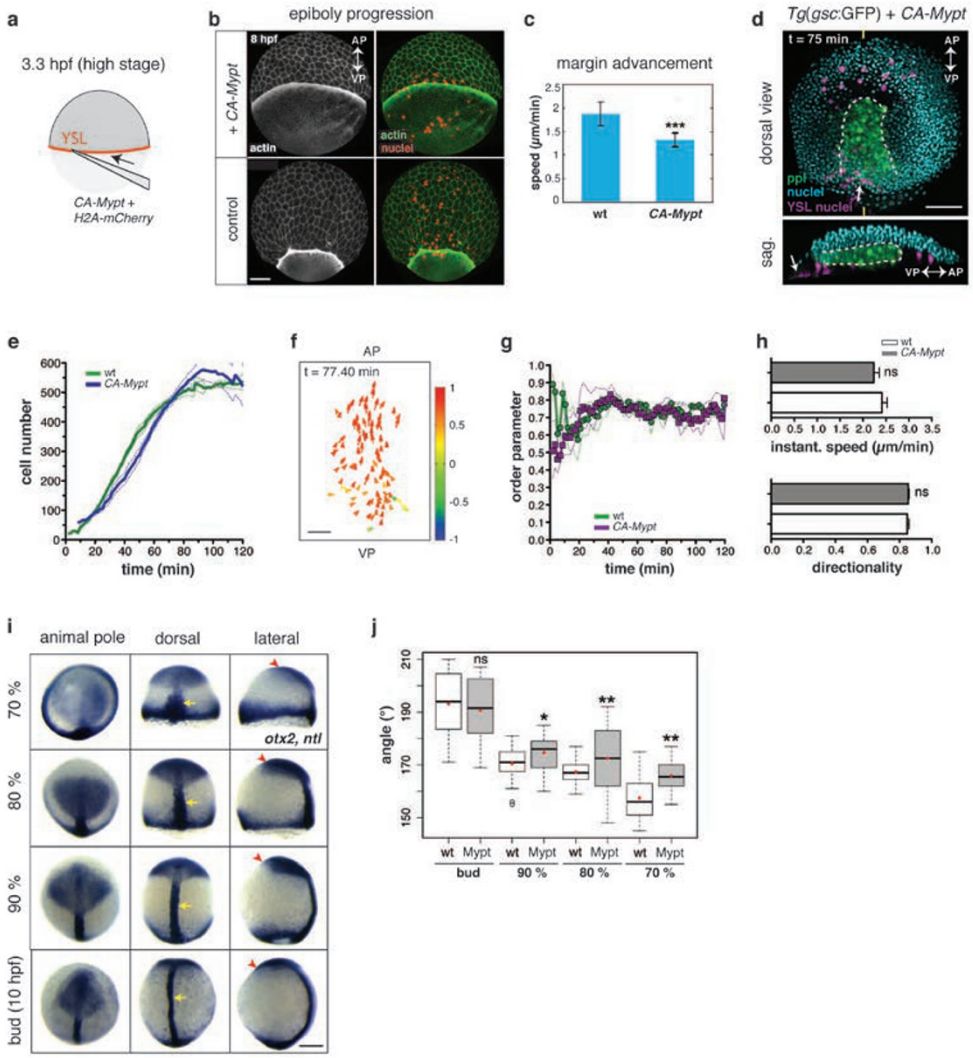

Supplementary Figure 4 Prechordal plate cell movements and neural plate positioning in wild type embryos overexpressing CA-Mypt within the yolk syncytial layer. (a) Schematic illustration of *CA-Mypt* and *H2A-mCherry* mRNA injection into the yolk syncytial layer (YSL) of an embryo at high stage (3.3 hpf). (b) Confocal images of the enveloping layer (EVL)/YSL epiboly progression in F-actin labeled *Tg(actb1:*GFP-UtrCH*)* wild type (wt) control (lower panel) and embryos injected with constitutively active myosin II phosphatase mRNA into the YSL (CA-Mypt, upper panel) at 8 hpf; both embryos were co-injected with *H2A-mCherry* mRNA into the YSL to mark YSL nuclei. (c) Quantification of the average advancement (µm/min) of the EVL margin of wt control and *CA-Mypt* injected embryos between 7 and 9 hpf; student's t-test; ***, P <0.001; n= 4 embryos; error bars, s.e.m. (d) Fluorescence images of a *Tg(gsc:*GFP*)* embryo overexpressing CA-Mypt and H2A-mCherry (magenta, arrows) within the YSL, also showing H2A-BFP expression within all nuclei and GFP-expression in *gsc*-expressing prechordal plate (ppl) progenitors (green, white outline) at a representative time point during gastrulation (t = 75 min, 6.25 hpf); dorsal and sagittal (dorsal up) sections through the embryo (yellow tags in upper panel mark sagittal section plane in lower panel); animal (AP) and vegetal pole (VP) indicated by arrows; scale bar, 100µm. (e) Number of internalized ppl cells in *Tg(gsc:*GFP*)* embryos overexpressing CA-Mypt within the YSL (blue curve, n = 4 embryos) versus wt embryos (green curve) plotted from 6 to 8 hpf (120 min); error bars, s.e.m. (f) Directional correlation of ppl cell movements in a wt embryo overexpressing CA-Mypt within the YSL at a representative time point during gastrulation (t = 77.40 min, 6.8 hpf); ppl cells are visualized as arrows in a 2D plot and color-coded according to their 3D correlation values between 1 (red, maximum correlation) and -1 (blue, minimum correlation); every 3rd cell is plotted; AP, animal pole; VP, vegetal pole; scale bar, 50 µm. (g) Average degree of alignment of ppl movements in embryos overexpressing CA-Mypt within the YSL (magenta curve/squares, n = 3 embryos) versus wt embryos (green curve/dots, see Supplementary Fig. 1c) plotted from 6 to 8 hpf (120 min); the order parameter corresponds to the degree of alignment ranging from 0 (disordered movement) to 1 (highly ordered movement); error bars, s.e.m. (h) Mean ppl cell instantaneous speed and directionality in CA-Mypt injected [gray bar graphs, n = 4 embryos; *P(speed)* = 0.323, *P(dir)* = 0.702] versus wt (white bar graphs, see Supplementary Fig. 2d) embryos plotted over 120min (6 to 8 hpf) as bar graphs; error bars, s.e.m.; student's t-test for all graphs; ns (not-significant), $P > 0.05$. (i) Anterior neural anlage in embryos overexpressing CA-Mypt within the YSL marked by whole-mount *in situ* hybridization of *otx2* mRNA expression at consecutive stages of gastrulation from 70% epiboly to bud stage (7 - 10hpf); posterior axial mesoderm was detected by *no tail (ntl)* mRNA expression (yellow arrows); animal pole (dorsal down), dorsal (animal pole up) and lateral (dorsal right) views are shown; red arrowhead marks the most anterior edge of the neural plate; 200 µm. (j) Quantitative analysis of neural plate position during gastrulation in embryos overexpressing CA-Mypt in the YSL versus wt embryos. The angle (°) between the vegetal pole and the anterior border of the otx2 expression domain was measured for embryos at different stages during gastrulation (i) and plotted as box-whisker graphs; n, embryos analyzed from 4 independent experiments; student's t-test (P value indicated) for all graphs comparing same stages; **, P<0.01; *, P<0.05, (ns) non significant, P >0.05; n (wt, bud) = 36, n (wt, 90%) = 36, n (wt, 70%) = 29, n (CA-Mypt, bud; P = 0.49) = 16, n (CA-Mypt, 90%; P = 0.0259) = 22, n (CA-Mypt, 80%; P = 0.0016) = 34, n (CA-Mypt, 70%; P = 0.0016) = 12; red dots mark mean values; box plot centre, median; red dot, mean; upper whisker, maximum; lower whisker, minimum.

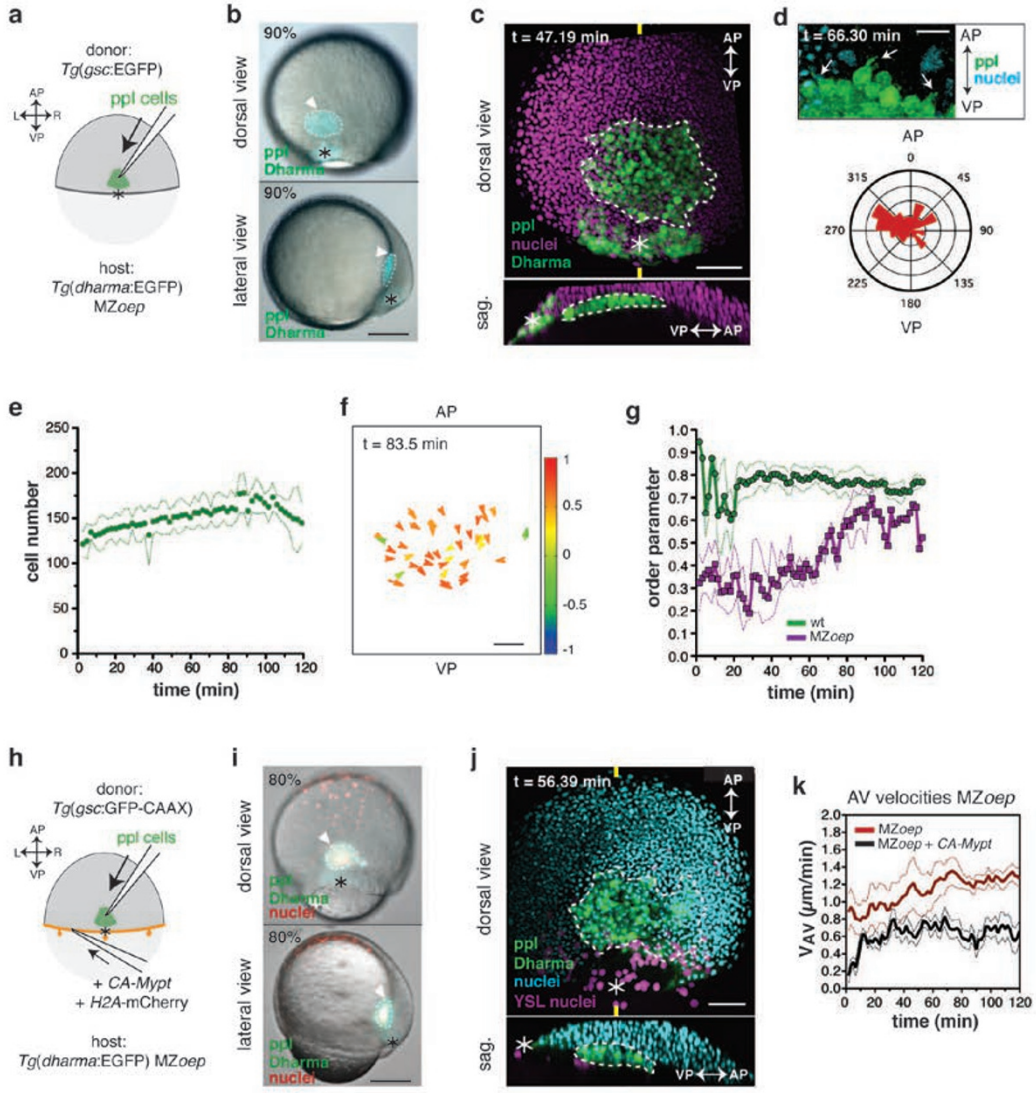

Supplementary Figure 5 Movement of transplanted prechordal plate cells in MZ*oep* mutant embryos. (a, h) Schematic illustration of a MZ*oep*;*Tg(dharma:*EGFP*)* (a) and a MZ*oep*;*Tg(dharma:*EGFP*)* mutant embryo that was injected with *CA-Mypt* mRNA into the YSL at high stage (h; 3.3 hpf) transplanted with prechordal plate (ppl) cells (green) into the dorsal side at 60% epiboly (6 hpf); asterisk marks position of dorsal marker Dharma; orange arrows indicate reduced vegetal-directed movement of EVL margin (h); AP, animal pole; VP, vegetal pole; L, left; R, right. (b, i) Bright-field/fluorescence image of a MZ*oep*;*Tg(dharma:*EGFP*)* mutant embryo at 90% epiboly (9 hpf) and a MZ*oep*;*Tg(dharma:*EGFP*)* mutant embryo at 80 % epiboly (8 hpf) that overexpresses CA-Mypt and the nuclei marker H2A-mCherry (red) within the YSL containing transplanted GFP-labeled ppl cells from *Tg(gsc:*GFP*)* donor (b) and *Tg(gsc:*GFP-CAAX*)* donor (i) embryos; ppl cell nuclei are marked by H2A-mCherry (i; red, co-localizes with green ppl cells); dashed white line indicates position of transplanted ppl progenitors; arrowhead points at anterior edge of ppl cells; asterisk marks *dharma:*EGFP signal at the dorsal side of the embryo; dorsal (animal pole up, top panel) and lateral (dorsal right, bottom panel) views; scale bar, 200 µm. (c, j) Fluorescence images of representative time points during gastrulation (c; t = 47.19 min, 6.8 hpf and j; t = 56.39 min, 6.9 hpf) showing a MZ*oep*;*Tg(dharma:*EGFP*)* (c) and a MZ*oep*;*Tg(dharma:*EGFP*)* mutant embryo which overexpresses CA-Mypt and the nuclei marker H2A-mCherry (magenta) within the YSL (j) containing transplanted *gsc*-expressing GFP-labeled ppl cells (white outline) from *Tg(gsc:*GFP*)* donor (c) and *Tg(gsc:*GFP-CAAX*)* donor (j) embryos; all nuclei are marked by H2A-mCherry (c; magenta) and H2A-BFP (j; cyan) expression, and the dorsal side of the embryos is marked by *dharma:*EGFP expression (green, asterisk); dorsal and sagittal (dorsal up) sections through the embryo (yellow tags in upper panel mark sagittal section plane in lower panel); animal pole (AP) and vegetal pole (VP) indicated by arrows; scale bar, 100µm. (d) Protrusion orientation of ppl cells transplanted into MZ*oep* mutants: top panel, fluorescence image of ppl cells with cytoplasm in green (*gsc:*GFP) and nuclei in cyan (H2A-BFP); animal pole up; scale bar, 20 µm. Bottom panel, polar plot or protrusion orientation of transplanted ppl cells (n = 48 cells from 2 embryos) with 0 ° = animal pole, 180 ° = vegetal pole. (e) Number of ppl cells transplanted into MZ*oep* mutant embryos (n=3 embryos) plotted from 6 to 8 hpf (120 min); error bars, s.e.m. (f) Directional correlation of transplanted ppl cell movements in a MZ*oep* mutant embryo at a representative time point during gastrulation (t = 83.5 min, 7.4 hpf); ppl cells are visualized as arrows in a 2D plot and color-coded according to their 3D correlation values between 1 (red, maximum correlation) and -1 (blue, minimum correlation); every 5th cell is plotted; AP, animal pole; VP, vegetal pole; scale bar, 50 µm. (g) Average degree of alignment of transplanted ppl cell movements in MZ*oep* mutant embryos (magenta curve/squares, n=3 embryos) versus endogenous ppl cell movements in wt embryos (green curve/dots, see Supplementary Fig. 2c) from 6 to 8 hpf (120 min); the order parameter corresponds to the degree of alignment ranging from 0 (disordered movement) to 1 (highly ordered movement); error bars, s.e.m. (k) Mean neurectoderm cell velocities along the animal-vegetal (AV) axis (V_{AV}) (measurement area indicated by black box in Supplementary Fig. 2e) in MZ*oep* mutant embryos (red curve, n=3 embryos) and MZ*oep* mutant embryos overexpressing CA-Mypt in the YSL (black curve, n=3 embryos); error bars, s.e.m.

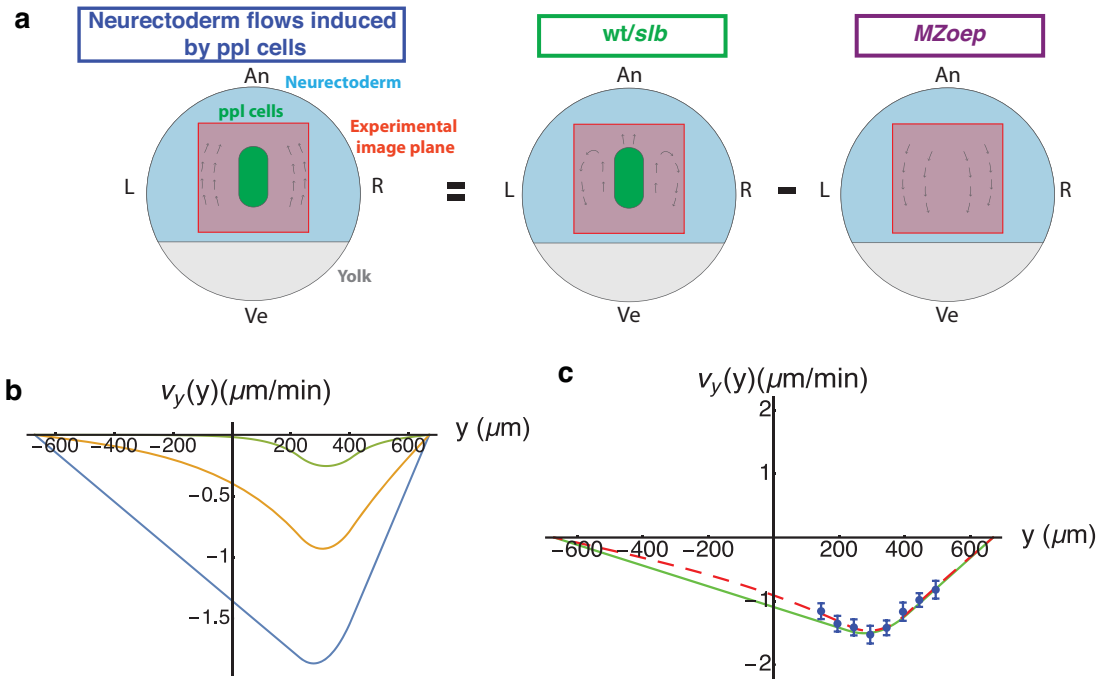

Supplementary Figure 6 Effect of external friction on one-dimensional neurectoderm flow profile. (a) For capturing the flow profile induced solely by prechordal plate (ppl) cells, MZoep mutants devoid of ppl cells were used to measure unperturbed epiboly movements, and those movements were subtracted from the overall neurectoderm flow field in wt embryos. This allowed decomposing the neurectoderm flow field and obtaining the ppl-induced movement alterations only. In the 2D description, neurectoderm flows exclusively within the experimental image plane (red square) were taken into account.(b) Theoretical 1D flow profile when the external friction coefficient ξ_0 between neurectoderm and tissues other than the ppl, such as the yolk cell and/or EVL, is varied. In case the external friction coefficient is increased, the range of flow triggered by ppl cells is decreased (blue: $\xi_0/\eta = 10^{-11}\mu m^{-2}$, orange: $\xi_0/\eta = 10^{-5}\mu m^{-2}$, green: $\xi_0/\eta = 10^{-4}\ \mu m^{-2}$, all curves: $f/\eta = -4.3\cdot10^{-5}\ \mu m^{-1}\cdot min^{-1}$). (c) Experimental velocities in wt embryos (blue dots) compared to theoretical flow profiles for the parameter settings as used in Fig. 5 (red dotted line, $f/\eta = -4.3\cdot10^{-5}\ \mu m^{-1}\cdot min^{-1}, \xi_0/\eta = 2.4\cdot10^{-6}\ \mu m^{-2}$), and for zero external friction (green line, $f/\eta = -3.5\cdot10^{-5}\ \mu m^{-1}\cdot min^{-1}, \xi_0/\eta = 0$). The experimental velocity profile in wt embryos is well explained by either a small ($\xi_0 < \eta/L_E^2$) or vanishing ($\xi_0 = 0$) external friction coefficient.

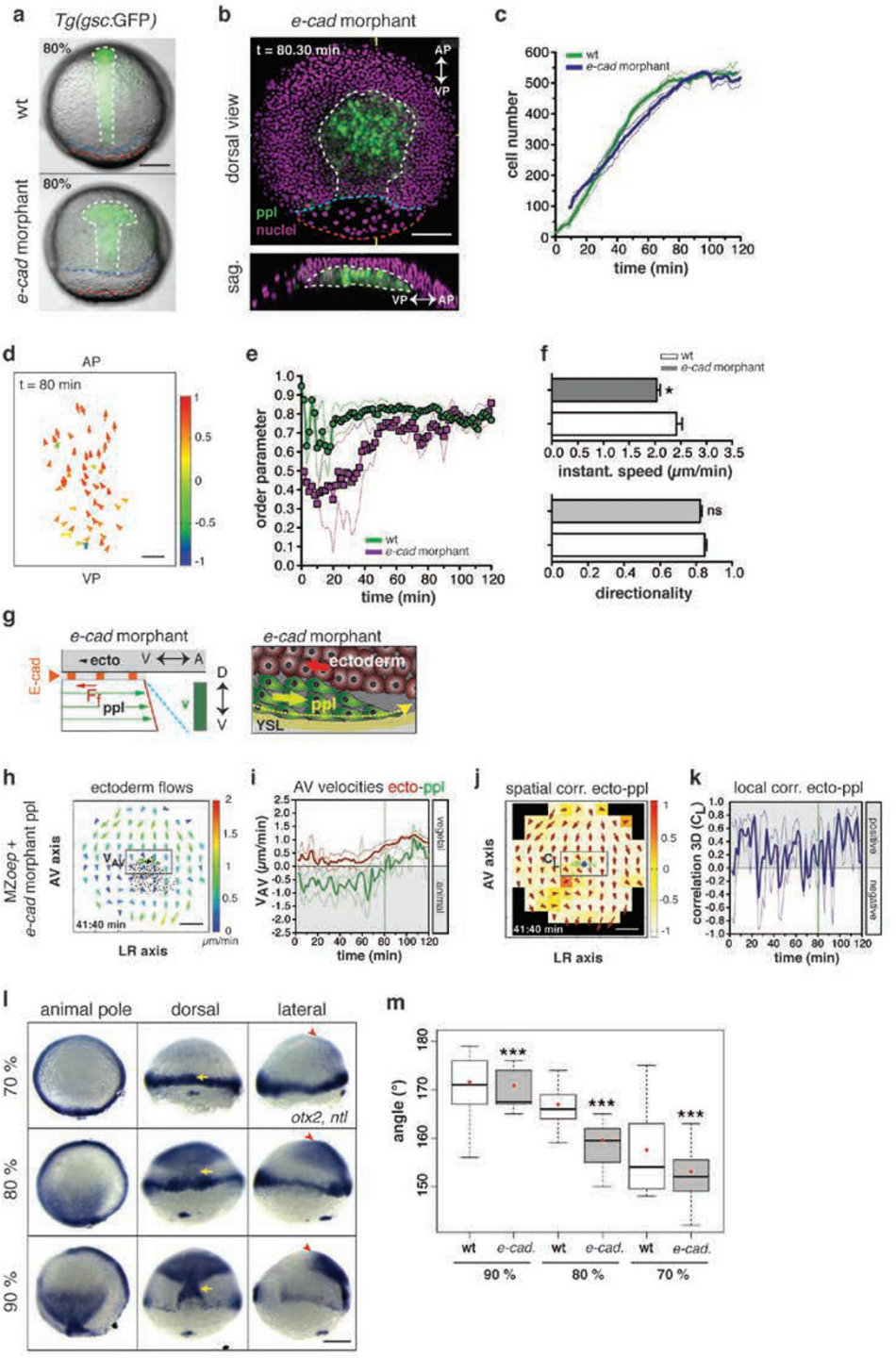

Supplementary Figure 7

Supplementary Figure 7 Prechordal plate cell movements and neural plate positioning in *e-cadherin* morphant embryos. (a) Brightfield/fluorescence image of a wild type (wt) *Tg(gsc:*GFP*)* (top panel) and *e-cadherin* (*e-cad*) morphant embryo (bottom panel) with *gsc*-expressing GFP-labeled prechordal plate progenitor (ppl) cells (green, white outline) at 80% epiboly; dorsal views, animal pole up; the increasing distance between the margins of the enveloping layer (EVL; red dashed line) and deep cell/neurectoderm (blue dashed line) shows (neur)ectoderm epiboly delay in *e-cad* morphant embryos; scale bar, 200 µm. (b) Fluorescence images of a *Tg(gsc:*GFP*)* *e-cad* morphant embryo showing H2A-mCherry (magenta) expression in all nuclei and GFP (green) expression in ppl cells (white outline) at a representative time point during gastrulation (t = 80.30 min, 7.3 hpf); dorsal and sagittal (dorsal up) sections through the embryo (yellow tags in upper panel mark sagittal section plane in lower panel); red and blue dashed lines as in (A); animal pole (AP) and vegetal pole (VP) indicated by arrows; scale bar, 100 µm. (c) Number of internalized ppl cells in *Tg(gsc:*GFP*)* *e-cad* morphant (blue curve, n=4 embryos) versus wt (green curve) embryos plotted from 6 to 8 hpf (120 min); error bars, s.e.m. (d) Correlation of ppl cell movements in a *e-cad* morphant embryo at a representative time point during gastrulation (t = 80 min, 7.3 hpf); ppl cells are visualized as arrows in a 2D plot and color-coded according to their 3D correlation values between 1 (red, maximum correlation) and -1 (blue, minimum correlation); every 3rd cell is plotted; AP, animal pole; VP, vegetal pole; scale bar, 50 µm. (e) Average degree of alignment of ppl movements in *e-cad* morphant (magenta curve/squares, n=3) versus wt (green curve/dots, see Supplementary Fig. 2c) embryos from 6 to 8 hpf (120 min); the order parameter corresponds to the degree of alignment, ranging from 0 (disordered movement) to 1 (highly ordered movement); error bars, s.e.m. (f) Mean ppl instantaneous speed and directionality in *e-cad* morphant [gray bar graphs, n=4 embryos; *P(speed)* = 0.0362; *P(dir)* = 0.222] versus wt (white bar graphs, see Supplementary Fig. 2d) embryos plotted as bar graphs; error bars, s.e.m; student's t-test for all graphs; *, $P < 0.05$; (ns) non significant, $P > 0.05$. (g) Model of friction generation under E-cadherin reduced conditions (compare with wt in Fig. 6f) in *e-cadherin* morphant embryo leads to decreased friction at the ppl-to-neurectoderm (ecto) interface and to non-graded velocities within the ppl (left panel; F_f, friction force; orange dashes indicate remaining cadherin); reduced E-cadherin-mediated adhesion between ppl and neurectoderm leads to loss of frictional drag and vegetal-directed movements (red arrow) of neurectoderm cells (right panel; yellow arrows indicate ppl movement); double-sided arrows indicate embryonic axes, animal (A) to vegetal (V), dorsal (D) to ventral (V). (h) 2D tissue flow map indicating velocities (µm/min) of neurectoderm (ectoderm) cell movements along the AV (V_{AP}) and left-right (LR) (V_{LR}) axis at the dorsal side of a MZ*oep* embryo overexpressing CA-Mypt within the YSL and transplanted with *e-cad* morphant ppl cells (t = 41.40 min, 6.7 hpf) at a representative time point; average velocity vector for each defined area is indicated and color-coded ranging from 0 (blue) to 2 (red) µm/min; positions of all/leading edge ppl cells are marked by black/green dots; black boxed area was used for mean velocity measurements in (i); scale bar, 100 µm. (i) Mean movement velocities (µm/min) along the AV axis (V_{AV}) of ppl leading edge progenitor cells (green curve, left y-axis) and neurectoderm (ecto) cells positioned above the ppl leading edge (black boxed area in h; red curve, right y-axis) in MZ*oep* embryos overexpressing CA-Mypt within the YSL and transplanted with *e-cad* morphant ppl cells (n=4 embryos) plotted from 6 to 8 hpf; vertical dashed line indicates start of vegetal-directed movements of ppl cells; error bars, s.e.m. (j) 3D directional correlation values between leading edge ppl and adjacent neurectoderm (ecto) cells in MZ*oep* embryo overexpressing CA-Mypt within the YSL and transplanted with *e-cad* morphant ppl cells (t = 41.40 min, 6.7 hpf) at a representative time point during gastrulation; degree of correlation is color-coded ranging rom 1 (red, highest) to -1 (white, lowest); average neurectoderm velocities for each defined area are marked; black boxed area was used for local correlation measurements in (k); scale bar, 100 µm. (k) 3D directional correlation values between leading edge ppl and adjacent neurectoderm (ecto) cells (black boxed area in j) in MZ*oep* embryos overexpressing CA-Mypt within the YSL and transplanted with *e-cad* morphant ppl cells (n=4 embryos) plotted from 6 to 8 hpf; error bars, s.e.m. (l) Anterior neural anlage in *e-cad* morphant embryos marked by whole-mount *in situ* hybridization of *otx2* mRNA expression at consecutive stage during gastrulation from 70% to 90% epiboly (7 - 9hpf); posterior axial mesoderm was detected by *no tail (ntl)* mRNA expression (yellow arrows), animal pole (dorsal down), dorsal (animal pole up) and lateral (dorsal right) views are shown; red arrowheads mark the most anterior edge of the neural plate; scale bar, 200 µm. (m) Quantitative analysis of neural plate position during gastrulation in *e-cad* morphant versus wt embryos; the angle (°) between the vegetal pole and the anterior border of the *otx2* expression domain was measured for embryos at different stages (l) and plotted as box-whisker graphs; n, embryos analyzed from 4 independent experiments; student's t-test (*P* value indicated) for all graphs comparing same stages; ***, $P < 0.001$, (ns) non significant, $P > 0.05$; n (wt, 90%) = 36, n (wt, 80%) = 34, n (wt, 70%) = 29, n (*e-cad*, 90%; $P < 0.0001$) = 30, n (*e-cad*, 80%; $P < 0.0001$) = 37, n (*e-cad*, 70%; $P = 0.00036$) = 41; box plot centre, median; red dot, mean; upper whisker, maximum; lower whisker, minimum.

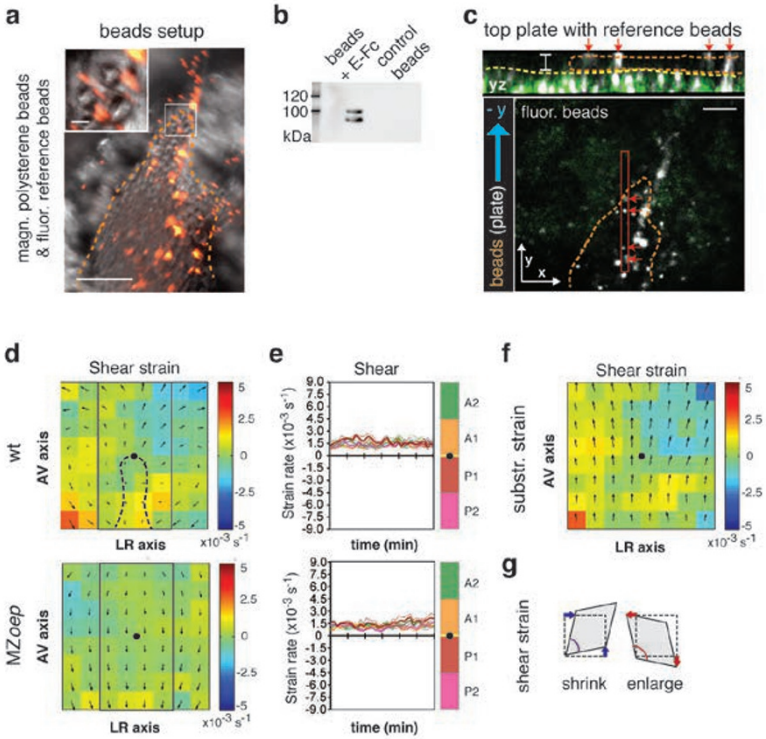

Supplementary Figure 8 Alterations in ectoderm movements upon application of E-cadherin mediated friction *ex vivo* and shear-strain-induced neurectoderm tissue deformation *in vivo*. (a) Bright-field/fluorescence image showing setup of magnetic polystyrene beads (20 µm diameter) and fluorescent reference beads (red, 4 µm diameter) attached to a glass plate used to apply friction onto ectoderm cells; dashed line outlines shape of polystyrene cluster; scale bars, 100 µm and 20 µm for magnified area. (b) Western Blot analysis showing detection of E-cadherin ectodomain (80 kDa) eluted from magnetic polystyrene beads coupled to E-cadherin-Fc Chimera (E-Fc) or uncoated control beads; molecular weight markers, 100 and 200 kDa. (c) Section of maximum projection confocal image (see Fig. 7a; t = 19.33 min) showing top plate with fluorescent reference beads and selected beads are highlighted (red arrows in xy and yz cross-section); cross-section (yz; red rectangle) shows the position of E-Fc-coated beads (outlined in orange) at the ectoderm cell interface (yellow dashed line); direction of beads movement (top plate; - y; velocity ~ 1.5 µm/min) is indicated; scale bars, 100µm in xy and 20 µm in yz. (d) Shear strain-induced neurectoderm tissue deformations of wild type (wt, upper panels; n=3 embryos) and MZ*oep* (lower panels; n=3 embryos) embryos plotted as time-averaged strain values for each domain (50 x 50 µm); average shear strain rate is color-coded according to amount of plane distortion [minimum green (0) to maximum red (5 x$10^{-3}s^{-1}$)]; tissue flows of neurectoderm are indicated as time-averaged velocities; dashed line indicates ppl and black dot marks ppl leading edge as reference point in wt and MZ*oep*; rectangle outlines area used for defining sectors along the animal-vegetal (AV) axis in (e). (e) Mean shear strain rates of neurectoderm tissue of wt (upper panels; n=3 embryos) and MZ*oep* (lower panels; n=3 embryos) in defined sectors (100 x 200 µm) are plotted along the AV axis over time of gastrulation (plotted from 6.3 to 7.3 hpf in 10 min intervals); sectors were positioned and color-coded relative to the ppl leading edge (anterior A1-2 and posterior P1-2 of the ppl leading edge; for detailed description refer to Supplementary Fig. 1e); amount of plane distortion [minimum green (0) to maximum red (10 x$10^{-3}s^{-1}$)] is plotted along the y-axis; (f) Neurectoderm tissue strain rate maps derived by subtraction of time-averaged shear strain values of wt from MZoep embryos (n=3 embryos); color-code as in (f); tissue flows of neurectoderm are indicated as time-averaged velocities; dashed line indicates ppl and black dot marks ppl leading edge as reference point. (g) Illustration of shear strain tissue deformation in the neurectoderm; arrows indicate direction of plane distortion of a tissue domain along the AV and left-right (LR) axis dependent on the direction and magnitude of neurectoderm movements; shear strain-induced domain angle of plane distortion can shrink (positive value) or enlarge (negative value).

Supplementary Video Legends

Supplementary Video 1 Live cell imaging of cell movements in wt embryo. Multiphoton time-lapse imaging of a wild type (wt) *Tg*(*gsc:*GFP) embryo with *gsc*-expressing GFP-labeled prechordal plate progenitor (ppl) cells (green) and neurectoderm cells at the dorsal side of the embryo from 6 to 8 hpf (123 min); all nuclei were labeled with histone H2A-BFP; animal/vegetal pole, up/down.

Supplementary Video 2 Life cell imaging of cell movements in MZ*oep* mutant embryo. Multiphoton time-lapse imaging of a MZ*oep*;*Tg*(*dharma*:EGFP) mutant embryo (Dharma:EGFP signal green) showing neurectoderm cells at the dorsal side of the embryo from 6 to 8.1 hpf (129 min); all nuclei were labeled with histone H2A-BFP; animal/vegetal pole, up/down.

Supplementary Video 3 2D velocities of neurectoderm cells in wt embryo. Tissue flow map indicating velocity vectors of neurectoderm cell movements along the animal-vegetal (AV) (V_{AV}) and left-right (LR) (V_{LR}) axis at the dorsal side of a wild type (wt) embryo between 6 to 8 hpf (117 min); average velocity vector for each defined area is indicated and color-coded ranging from 0 (blue) to 2 (red) µm/min; position of all/leading edge prechordal plate (ppl) cells are indicated as black/green dots; xy-axes in µm; time in mins; animal/vegetal pole, up/down.

Supplementary Video 4 3D correlation of neurectoderm and prechordal plate (pp) cell movements in wt embryo. Movement correlation between neurectoderm and underlying (ppl) cells at the dorsal side of a wild type (wt) embryo between 6 to 8 hpf (118 min); degree of correlation is color-coded ranging from 1 (red, highest correlation) to -1 (white, lowest correlation); average neurectoderm movement velocities and direction for each defined area are indicated by arrows; position of all/leading edge ppl cells are indicated as white/green dots; blue arrow marks movement direction of ppl leading edge cells; xy-axes in µm; time in mins; animal/vegetal pole, up/down.

Supplementary Video 5 2D velocities of neurectoderm cells in MZ*oep* mutant embryo. Tissue flow map indicating velocity vectors of neurectoderm cell movements along the animal-vegetal (AV) (V_{AV}) and left-right (LR) (V_{LR}) axis at the dorsal side of a MZ*oep* mutant embryo between 6 to 8 hpf (121 min); average velocity vector for each defined area is indicated and color-coded ranging from 0 (blue) to 2 (red) µm/min; xy-axes in µm; time in mins; animal/vegetal pole, up/down.

Supplementary Video 6 3D correlation of neurectoderm and prechordal plate (pp) cell movements in *CA-Mypt* injected embryo. Movement correlation between neurectoderm and underlying prechordal plate (ppl) cells at the dorsal side of a wt embryo overexpressing CA-Mypt in the YSL between 6 to 8 hpf (118 min); degree of correlation is color-coded ranging from 1 (red, highest correlation) to -1 (white, lowest correlation); average neurectoderm movement velocities and direction for each defined area are indicated by arrows; position of all/leading edge ppl cells are indicated as white/green dots; blue arrow marks movement direction of ppl leading edge cells; xy-axes in µm; time in mins; animal/vegetal pole, up/down.

Supplementary Video 7 2D velocities of neurectoderm cells in ppl-transplanted MZ*oep* mutant embryo. Tissue flow map indicating velocity vectors of neurectoderm cell movements along the animal-vegetal (AV) (V_{AV}) and left-right (LR) (V_{LR}) axis at the dorsal side of a transplanted MZ*oep* mutant embryo between 6 to 7.5 hpf (91 min); average velocity vector for each defined area is indicated and color-coded ranging from 0 (blue) to 2 (red) µm/min; position of all/leading edge transplanted prechordal plate (ppl) cells are indicated as black /green dots; xy-axis in µm; time in mins; animal/vegetal pole, up/down.

Supplementary Video 8 2D velocities of neurectoderm cells in ppl-transplanted and *CA-Mypt* injected MZ*oep* mutant embryo. Tissue flow map indicating velocity vectors of neurectoderm cell movements along the animal-vegetal (AV) (V_{AV}) and left-right (LR) (V_{LR}) axis at the dorsal side of a MZ*oep* embryo overexpressing CA-Mypt within the YSL between 6 to 8 hpf (120 min); average velocity vector for each defined area is indicated and color-coded ranging from 0 (blue) to 2 (red) µm/min; position of all/leading edge transplanted prechordal plate (ppl) cells are indicated as black /green dots; xy-axis in µm; time in mins; animal/vegetal pole, up/down.

Supplementary Video 9 Arrangement of leading and trailing prechordal plate (ppl) cells in wild type (wt) embryo. Consecutive z-sections of a fluorescent imaging stack showing lifeact-GFP (F-actin) expressing ppl cells transplanted into the ppl leading edge of a wt embryo expressing Utrophin-mCherry (F-actin) and H2A-mCherry (nuclei); section starts at the ppl-neurectoderm interface and progresses through the leading edge ppl to the ppl-YSL interface; animal pole to the left; z-section taken from movie 16 at t = 12.36 min; scale bar, 20 µm.

Supplementary Video 10 Life cell imaging of leading and trailing prechordal plate (ppl) cells in wild type (wt) embryo. Fluorescence time-lapse imaging of lifeact-GFP (F-actin) expressing ppl cells transplanted into the ppl leading edge of a wt embryo expressing Utrophin-mCherry (F-actin) and H2A-mCherry (nuclei) starting at 70% epiboly (7 hpf); dorsal (top, animal pole left) and sagittal (bottom, animal pole left) sections through the embryo with dual (left side) and single (right side) color label; time in mins; scale bar, 20 µm.

Supplementary Video 11 2D velocities of neurectoderm cells in *e-cadherin* morphant embryo. Tissue flow map indicating velocity vectors of neurectoderm cell movements along the animal-vegetal (AV) (V_{AV}) and lefty-right (LR) (V_{LR}) axis at the dorsal side of a *e-cadherin* morphant embryo between 6 to 8 hpf (120 min); average velocity vector for each defined area is indicated and color-coded ranging from 0 (blue) to 2 (red) µm/min; position of all/leading edge prechordal plate (ppl) cells are indicated as black /green dots; xy-axis in µm; time in mins; animal/vegetal pole, up/down.

Supplementary Video 12 3D correlation of neurectoderm and prechordal plate (ppl) cell movements in *e-cadherin* morphant embryo. 3D movement correlation between neurectoderm and underlying prechordal plate (ppl) cells at the dorsal side of *e-cadherin* morphant embryo 6 to 8 hpf (120 min); degree of correlation is color-coded ranging from 1 (red, highest correlation) to -1 (white, lowest correlation); average neurectoderm movement velocities and direction for each defined area are indicated by arrows; position of all/leading edge ppl cells are indicated as white/green dots; blue arrow marks movement direction of ppl leading edge cells; xy-axes in µm; time in mins; animal/vegetal pole, up/down.

SUPPLEMENTARY NOTE

In these supplementary informations we propose a theoretical description of flows arising in the neurectoderm as a result of the underlying motion of ppl cells. In order to analyze the specific effect of ppl cells on neurectoderm flows, we use experimental measurements of neuroectoderm velocity field in the presence of ppl cells, denoted $\mathbf{v}^{\rm tot}$, and experimental measurements of neuroectoderm velocity field in the absence of ppl cells in MZ*oep* mutants (denoted $\mathbf{v}^{\rm MZ}$). We then calculate the difference between these velocity fields:

$$\mathbf{v} = \mathbf{v}^{\rm tot} - \mathbf{v}^{\rm MZ}. \tag{1}$$

Our theoretical description aims at reproducing this velocity field.

1. Simplified one dimensional description of neurectoderm flows

We describe the neurectoderm as a two-dimensional viscous compressible fluid, flowing with velocity vector $\mathbf{v}$. We assume that the effect of ppl cells is to exert an external force on the neuroectoderm, and we analyze the flow profile induced by this external force.

1.1. **Main equation of one-dimensional viscous flow.** We first discuss a simplified description of the flow in one dimension. We aim here at understanding flow profiles measured along the animal-vegetal axis of the embryo, with y denoting the coordinate along the animal-vegetal axis, going positively towards the vegetal axis (Fig. 5a). We consider the velocity towards the vegetal pole v_y, and the tension within the tissue is denoted σ_y. We consider the tissue to be fluid with effective one-dimensional viscosity $\bar{\eta}$, such that the stress within the tissue reads

$$\sigma_y = \bar{\eta}\partial_y v_y \tag{2}$$

We assume that neurectoderm cells flow with a friction coefficient ξ_0 relative to the surrounding tissues other than ppl cells. For instance, ξ_0 could be caused by relative friction between the neurectoderm and the EVL or by friction between the neurectoderm and the yolk. In addition, we assume that within the ppl domain, delimited by the region $y^{\rm ppl} - L_y^{\rm ppl} < y < y^{\rm ppl} + L_y^{\rm ppl}$,

ppl cells exert a uniform force density f. Force balance at low Reynolds number then reads:

$$\partial_y \sigma_y = \xi_0 v_y \quad \text{outside of ppl domain} \tag{3}$$

$$\partial_y \sigma_y = \xi_0 v_y - f \quad \text{inside the ppl domain} \tag{4}$$

Finally, we denote L^E the distance from the animal pole to the neurectoderm margin, such that $y = 0$ denotes the animal pole and $y = -L^E$ and $y = L^E$ denote the neurectoderm margin on the ventral and dorsal side. We impose that the flow vanishes at the margin, $v_y(-L^E) = v_y(L^E) = 0$. The solution for the flow reads:

$$v_y = C_1 \left(e^{\frac{y}{l_0}} - e^{-\frac{2L^E + y}{l_0}} \right) \quad , \quad y < y^{\text{ppl}} - L_y^{\text{ppl}} \tag{5}$$

$$v_y = C_2 e^{\frac{y}{l_0}} + C_3 e^{-\frac{y}{l_0}} + \frac{f}{\xi_0} \quad , \quad y^{\text{ppl}} - L_y^{\text{ppl}} < y < y^{\text{ppl}} + L_y^{\text{ppl}} \tag{6}$$

$$v_y = C_4 \left(e^{\frac{y}{l_0}} - e^{\frac{2L^E - y}{l_0}} \right) \quad , \quad y > y^{\text{ppl}} + L_y^{\text{ppl}} \tag{7}$$

with $l_0 = \sqrt{\bar{\eta}/\xi_0}$ an hydrodynamic length, and $C_i, i = 1, ..., 4$ are constants which can be determined from the conditions of continuity of the velocity and its derivative at the boundaries of the ppl domain. The flow profile induced by a localized external force decays exponentially away from the ppl region exponentially on the length l_0 (Supplementary Fig. 6b).

In the limit where friction acting on the tissue from other sources than ppl cells can be neglected, ($l_0 \gg L^E$), the solution for the flow profile reads:

$$v_y = \frac{f L_y^{\text{ppl}}}{\bar{\eta}} \left(1 - \frac{y^{\text{ppl}}}{L^E} \right) (L^E + y) \quad , \quad y < y^{\text{ppl}} - L_y^{\text{ppl}} \tag{8}$$

$$v_y = -\frac{f}{2\bar{\eta}} \left((y - y^{\text{ppl}})^2 + \frac{2L_y^{\text{ppl}} y^{\text{ppl}}}{L^E} (y - y^{\text{ppl}}) + \frac{L_y^{\text{ppl}}}{L^E} (2{y^{\text{ppl}}}^2 - 2{L^E}^2 + L^E L_y^{\text{ppl}}) \right) \quad , \quad y^{\text{ppl}} - L_y^{\text{ppl}} < y < y^{\text{ppl}} + L_y^{\text{ppl}} \tag{9}$$

$$v_y = \frac{f L_y^{\text{ppl}}}{\bar{\eta}} \left(1 + \frac{y^{\text{ppl}}}{L^E} \right) (L^E - y) \quad , \quad y > y^{\text{ppl}} + L_y^{\text{ppl}} \tag{10}$$

In that case the flow profile decays linearly towards the EVL margin.

1.2. **Comparison to experimental flow profile along the dorsal midline.**

1.2.1. *Wild-type velocity profiles.* To compare to experiment, we first aimed at matching theoretical profiles with wt velocity profiles along the animal-vegetal axis, on the dorsal line. Estimates of the lengths L^{ppl}, L^E and y^{ppl} used for comparison are discussed in section 3 and reported in Table 2.

A fitting procedure then gave $f/\bar{\eta} = -4.2 \cdot 10^{-5} \mu\mathrm{m}^{-1} \cdot \mathrm{min}^{-1}$ and $\bar{\eta}/\xi_0 = 6.3 \cdot 10^5 \mu\mathrm{m}^2$ (Table 1), corresponding to an hydrodynamic length $l_0 = 793$ μm. Because l_0 is close to the system size L^E, we conclude that external friction arising from other tissues than ppl cells has a small effect on the flow profile in wt. Predicted profiles without external friction from surrounding tissues ($\xi_0 = 0$) indeed also match experimental profiles closely (Supplementary Fig. 6c).

Assuming that the force density f exerted by ppl cells on the neuroectoderm can be described by a dynamic friction force, we then have the following relation:

$$f = \xi(v_y^{ppl} - v_y^{\mathrm{tot}}), \tag{11}$$

where v_y^{ppl} is the velocity of ppl cells, v_y^{tot} is the wild-type neuroectoderm total velocity at the same point and ξ is the friction coefficient. To determine the friction coefficient, we average Eq. 11 in the domain of ppl cells, assuming here for simplicity that the force density f is homogeneous within the ppl domain:

$$f = \xi(\langle v_y^{ppl} \rangle - \langle v_y^{\mathrm{tot}} \rangle). \tag{12}$$

We then estimate the experimental values of $\langle v_y^{ppl} \rangle$ and $\langle v_y^{\mathrm{tot}} \rangle$. The corresponding values are reported in Table 1. We then obtain an estimate of f/ξ, and using the value of $f/\bar{\eta}$ obtained by comparison with experimental profiles, we then can estimate the ratio $\bar{\eta}/\xi$ (Table 1). A characteristic hydrodynamic length can be defined from this ratio by:

$$l_1 = \sqrt{\bar{\eta}/\xi}. \tag{13}$$

Note that $l_1 \neq l_0$ since ξ is associated to friction acting in between the neurectoderm and ppl cells, while ξ_0 is associated to friction in between the neurectoderm and other tissues. We find $l_1 \simeq 288$ μm, corresponding to a friction coefficient about 8 times larger in between neurectoderm and ppl cells than in between neurectoderm and other tissues.

Simplified one-dimensional description							
Exp	$f/\bar{\eta}$	$\bar{\eta}/\xi_0$	$\langle v_y^{\rm ppl}\rangle$	$\langle v_y^{\rm tot}\rangle$	f/ξ	$\bar{\eta}/\xi$	l_1
Unit	μm$^{-1}\cdot$min^{-1}	μm^2	μm/min	μm/min	μm/min	μm^2	μm
wt	-4.2 $\cdot 10^{-5}$	6.3$\cdot 10^5$	-4	-0.5	-3.5	8.4$\cdot 10^4$	290
slb	-3.4 $\cdot 10^{-5}$	6.3$\cdot 10^5$	-2.5	0.4	-2.9	8.4$\cdot 10^4$	290
Two-dimensional description							
Exp	f/η_b	η_b/η	$\langle v_y^{\rm ppl}\rangle$	$\langle v_y^{\rm tot}\rangle$	f/ξ	η_b/ξ	l_2
Unit	μm$^{-1}\cdot$min^{-1}		μm/min	μm/min	μm/min	μm^2	μm
wt	-2 $\cdot 10^{-4}$	1	-4	-0.5	-3.5	1.8$\cdot 10^4$	133
slb	-1.6 $\cdot 10^{-4}$	1	-2.5	0.4	-2.9	1.8$\cdot 10^4$	133

Table 1. Values of parameters obtained by comparison of the one dimensional simplfied theory and two-dimensional theory with experiments.

1.3. ***slb* mutant velocity profiles.** ppl cells have a reduced velocity in *slb* mutants. We therefore estimate the reduction in the magnitude of ppl exerted force density f from Eq. 12, using experimentally measured average velocities in the ppl region (Table 1). We then obtain the corresponding predicted theory profile, keeping mechanical parameters other than f as in wt, and using geometrical parameters reported in Table 2. This yields a very good agreement with experimental profiles (Fig. 5-b1).

2. Two-dimensional flow

2.1. **Main equations.** We discuss here the two-dimensional flow profiles obtained in the region of experimental measurement, a square domain of size $2L$. For simplicity, we ignore the curvature of the embryo and use 2D cartesian coordinates x, y. For comparison with flows observed in the zebrafish embryo, the x axis is going on the surface of the embryo along the left-right direction, away from the dorsal midline of the embryo, and the y axis as going along the animal-vegetal direction, away from the animal pole. The corresponding geometry is represented in Fig. 5a. As before, we assume that the effect of ppl cells is to exert an external force on the neuroectoderm. We solve for the theoretical flow within the region of observation, and impose experimentally measured velocities at the boundary of the region.

Force balance on the neuroectoderm in two dimensions now reads

$$\partial_i \sigma_{ij} = -f_j^{\mathrm{ppl}}, \tag{14}$$

where σ_{ij} is the two-dimensional stress tensor within the neurectoderm, and $\mathbf{f}^{\mathrm{ppl}}$ is the two-dimensional force density exerted by ppl cells on the neurectoderm.

The stress tensor σ_{ij} in the neuroectoderm tissue reads:

$$\sigma_{ij} = 2\eta\Big[v_{ij} - \frac{1}{2}v_{kk}\delta_{ij}\Big] + \eta_b v_{kk}\delta_{ij}, \tag{15}$$

where η is the neurectoderm shear viscosity, η_b is the neurectoderm bulk viscosity, and $v_{ij} = (\partial_i v_j + \partial_j v_i)/2$ is the symmetric part of the gradient of flow.

We further choose the following form for the force density exerted by ppl cells:

$$\begin{aligned} f_j^{\mathrm{ppl}} &= f\left(\mathcal{H}[x + L_x^{\mathrm{ppl}}] - \mathcal{H}[x - L_x^{\mathrm{ppl}}]\right) \\ &\quad \times \left(\mathcal{H}[y - y^{\mathrm{ppl}} + L_y^{\mathrm{ppl}}] - \mathcal{H}[y - y^{\mathrm{ppl}} - L_y^{\mathrm{ppl}}]\right)\delta_{jy} \end{aligned} \tag{16}$$

where $\mathcal{H}$ is the Heaviside function. This choice corresponds to a uniform force density with magnitude f, acting along the y direction, and exerted on a rectangular domain of size $2L_x^{\mathrm{ppl}} \times 2L_y^{\mathrm{ppl}}$, centred around $x = 0$ and $y = y^{\mathrm{ppl}}$.

By using the constitutive equation 15, the force balance equation 14, and the force density 16, we obtain the following equation for the flow field:

$$\begin{cases} \eta\Delta v_x + \eta_b(\partial_x^2 v_x + \partial_y\partial_x v_y) = 0, \\ \eta\Delta v_y + \eta_b(\partial_y^2 v_y + \partial_y\partial_x v_x) = -f\left(\mathcal{H}[x + L_x^{\mathrm{ppl}}] - \mathcal{H}[x - L_x^{\mathrm{ppl}}]\right) \\ \qquad\qquad \times \left(\mathcal{H}[y - y^{\mathrm{ppl}} + L_y^{\mathrm{ppl}}] - \mathcal{H}[y - y^{\mathrm{ppl}} - L_y^{\mathrm{ppl}}]\right). \end{cases} \tag{17}$$

Eqs. 17 are then solved on a rectangular domain of size $2L \times 2L$. The boundary conditions are set by imposing experimentally measured velocity profiles

$$v_x(L, y) = v_x^{R,\exp}(y), \quad v_y(L, y) = v_y^{R,\exp}(y) \tag{18}$$

$$v_x(-L, y) = v_x^{L,\exp}(y), \quad v_y(-L, y) = v_y^{L,\exp}(y) \tag{19}$$

$$v_x(x, L) = v_x^{U,\exp}(x), \quad v_y(x, L) = v_y^{U,\exp}(x) \tag{20}$$

$$v_x(x, -L) = v_x^{D,\exp}(x), \quad v_y(x, -L) = v_y^{D,\exp}(x). \tag{21}$$

2.2. **Calculation of flow fields.** To solve for the velocity field and get explicit expressions for v_x and v_y, we used the method of superposition. For convenience, we used the following decomposition of the velocity field:

$$\begin{aligned} v_x(x,y) &= v_x^{\mathrm{per}}(x,y) + \sum_{n=1}^{N} \alpha_n(y) \sin\left(\frac{n\pi(x-L)}{2L}\right) \\ &\quad + \sum_{n=1}^{N} \beta_n(x) \cos\left(\frac{n\pi(y-L)}{2L}\right) + \beta_0(x) \end{aligned} \tag{22}$$

$$\begin{aligned} v_y(x,y) &= v_y^{\mathrm{per}}(x,y) + \sum_{n=1}^{N} \gamma_n(y) \cos\left(\frac{n\pi(x-L)}{2L}\right) \\ &\quad + \sum_{n=1}^{N} \delta_n(x) \sin\left(\frac{n\pi(y-L)}{2L}\right) + \gamma_0(y) \end{aligned} \tag{23}$$

In the equation above, $v_x^{\mathrm{per}}(x,y)$ and $v_y^{\mathrm{per}}(x,y)$ are solution of Eq. 17 which are periodic along the x axis and have vanishing velocities at the boundaries $y=-L$ and $y=L$. The additional truncated Fourier sums are introduced to verify the remaining boundary conditions.

2.2.1. *Determination of the periodic solution.* To obtain the periodic solution, we introduce the Fourier transforms of the velocity field along the x direction:

$$\begin{cases} \tilde{v}_x(k_x,y) = \frac{1}{\sqrt{2\pi}} \int dx e^{-ik_x x} v_x^{\mathrm{per}}(x,y) \\ \tilde{v}_y(k_x,y) = \frac{1}{\sqrt{2\pi}} \int dx e^{-ik_x x} v_y^{\mathrm{per}}(x,y). \end{cases} \tag{24}$$

where $k_x = \pi n/L$ with $n \in \mathbb{Z}$. We then obtain from Eq. 17:

$$\begin{cases} \eta \partial_y^2 \tilde{v}_x + \eta_b i k_x \partial_y \tilde{v}_y - (\eta+\eta_b) k_x^2 \tilde{v}_x = 0 \\ (\eta+\eta_b)\partial_y^2 \tilde{v}_y + \eta_b i k_x \partial_y \tilde{v}_x - \eta k_x^2 \tilde{v}_y = C(k_x)\mathcal{H}_y, \end{cases} \tag{25}$$

where we have introduced $C(k_x) = -f\sqrt{\frac{2}{\pi}}\frac{sin(k_x L_x^{\mathrm{ppl}})}{k_x}$ for $k_x \neq 0$ and $C(0) = -f\sqrt{2/\pi}L_x^{\mathrm{ppl}}$, and $\mathcal{H}_y = \mathcal{H}[y - y^{\mathrm{ppl}} + L_y^{\mathrm{ppl}}] - \mathcal{H}[y - y^{\mathrm{ppl}} - L_y^{\mathrm{ppl}}]$. These equations can be rewritten after rearrangement

$$\begin{cases} \partial_y^4 \tilde{v}_x - 2k_x^2 \partial_y^2 \tilde{v}_x + k_x^4 \tilde{v}_x = -\frac{C(k_x)\eta_b i k_x \mathcal{H}_y'}{\eta(\eta+\eta_b)} \\ \partial_y^4 \tilde{v}_y - 2k_x^2 \partial_y^2 \tilde{v}_y + k_x^4 \tilde{v}_y = \frac{C(k_x)\mathcal{H}_y''}{\eta+\eta_b} - \frac{C k_x^2 \mathcal{H}_y}{\eta}. \end{cases} \tag{26}$$

We solve separately these equations in the following three domains (1), $-L_y^{\rm ppl} < y < L_y^{\rm ppl}$; (2), $y > L_y^{\rm ppl}$, (3), $y < -L_y^{\rm ppl}$, and the corresponding solutions read for $k_x \neq 0$:

$$\begin{cases} \tilde{v}_x^1 = (D_1 + D_2 y)e^{k_x y} + (D_3 + D_4 y)e^{-k_x y} \\ \tilde{v}_y^1 = \left[\frac{i}{\eta_b k_x}(2\eta + \eta_b)D_2 - iD_1 - iD_2 y\right]e^{k_x y} + \left[\frac{i}{\eta_b k_x}(2\eta + \eta_b)D_4 + iD_3 + iD_4 y\right]e^{-k_x y} - \frac{C(k_x)}{\eta k_x^2} \\ \tilde{v}_x^2 = (G_1 + G_2 y)e^{k_x y} + (G_3 + G_4 y)e^{-k_x y} \\ \tilde{v}_y^2 = \left[\frac{i}{\eta_b k_x}(2\eta + \eta_b)G_2 - iG_1 - iG_2 y\right]e^{k_x y} + \left[\frac{i}{\eta_b k_x}(2\eta + \eta_b)G_4 + iG_3 + iG_4 y\right]e^{-k_x y} \\ \tilde{v}_x^3 = (M_1 + M_2 y)e^{k_x y} + (M_3 + M_4 y)e^{-k_x y} \\ \tilde{v}_y^3 = \left[\frac{i}{\eta_b k_x}(2\eta + \eta_b)M_2 - iM_1 - iM_2 y\right]e^{k_x y} + \left[\frac{i}{\eta_b k_x}(2\eta + \eta_b)M_4 + iM_3 + iM_4 y\right]e^{-k_x y}. \end{cases} \tag{27}$$

where we have introduced 12 constants D_i, G_i, M_i, that can be determined from boundary conditions. Using the boundary conditions of vanishing velocity at the boundaries $y = -L$ and $y = L$, together with the continuity of the velocity field v_x, v_y and of the stress components σ_{xy} and σ_{yy} at the interfaces $y = L_y^{\rm ppl}$ and $y = -L_y^{\rm ppl}$, we obtain a system of equations that allow to determine all the constants. For $k_x = 0$, the solution reads

$$\begin{cases} \tilde{v}_x = 0 \\ \tilde{v}_y^1 = -\sqrt{\frac{2}{\pi}}\frac{f L_x^{\rm ppl}}{2(\eta+\eta_b)} y^2 + K_1 y + K_2 \\ \tilde{v}_y^2 = W_1 y + W_2 \\ \tilde{v}_y^3 = Z_1 y + Z_2. \end{cases} \tag{28}$$

The 6 constants K_i, W_i and Z_i are determined from the boundary conditions imposing the continuity of the velocity at the ppl boundary, the continuity of the stress σ_{yy} at the ppl boundary, and zero v_y velocity at the domain boundary.

From the solution in Fourier space, the real-space solution is then obtained from

$$\begin{cases} v_x^{\rm per}(x,y) = \frac{1}{\sqrt{2\pi}}\frac{\pi}{L}\sum_{k_x} e^{ik_x x}\tilde{v}_x(k_x,y), \\ v_y^{\rm per}(x,y) = \frac{1}{\sqrt{2\pi}}\frac{\pi}{L}\sum_{k_x} e^{ik_x x}\tilde{v}_y(k_x,y). \end{cases} \tag{29}$$

where the sum is numerically performed in practice for $0 < n < N_{max}$. In the results reported here, we chose $N_{max} = 400$.

2.2.2. *Determination of the remaining solution of the homogeneous equation.* The remaining part of the solution $\bar{v}_x = v_x - v_x^{\rm per}$ and $\bar{v}_y = v_y - v_y^{\rm per}$ verifies the homogeneous equation

$$\eta\Delta\bar{v}_x + \eta_b(\partial_x^2\bar{v}_x + \partial_y\partial_x\bar{v}_y) = 0, \tag{30}$$

$$\eta\Delta\bar{v}_y + \eta_b(\partial_y^2\bar{v}_y + \partial_y\partial_x\bar{v}_x) = 0. \tag{31}$$

We find that these equations are satisfied using the following form for the undetermined functions in Eq. 22:

$$\alpha_n(y) = (A_1^n + A_2^n y)e^{-\frac{n\pi y}{2L}} + (A_3^n + A_4^n y)e^{\frac{n\pi y}{2L}} \tag{32}$$

$$\gamma_n(y) = (a_n A_2^n + A_1^n + A_2^n y)e^{-\frac{n\pi y}{2L}} + (a_n A_4^n - A_3^n - A_4^n y)e^{\frac{n\pi y}{2L}} \tag{33}$$

$$\beta_n(x) = (a_n D_2^n + D_1^n + D_2^n x)e^{-\frac{n\pi x}{2L}} + (a_n D_4^n - D_3^n - D_4^n x)e^{\frac{n\pi x}{2L}} \tag{34}$$

$$\delta_n(x) = (D_1^n + D_2^n x)e^{-\frac{n\pi x}{2L}} + (D_3^n + D_4^n x)e^{\frac{n\pi x}{2L}} \tag{35}$$

$$\beta_0(x) = D_1^0 + D_2^0 x \tag{36}$$

$$\gamma_0(y) = A_1^0 + A_2^0 y. \tag{37}$$

with $a_n = (2L(2\eta + \eta_b)/(n\pi\eta_b))$.

We then impose the boundary conditions for $\bar{v}_x, \bar{v}_y$:

$$\bar{v}_x(L, y) = \bar{v}_x^{R,\exp}(y) = v_x^{R,\exp}(y) - v_x^{\rm per}(L, y) \tag{38}$$

$$\bar{v}_y(L, y) = \bar{v}_y^{R,\exp}(y) = v_y^{R,\exp}(y) - v_y^{\rm per}(L, y) \tag{39}$$

$$\bar{v}_x(-L, y) = \bar{v}_x^{L,\exp}(y) = v_x^{L,\exp}(y) - v_x^{\rm per}(-L, y) \tag{40}$$

$$\bar{v}_y(-L, y) = \bar{v}_y^{L,\exp}(y) = v_y^{L,\exp}(y) - v_y^{\rm per}(-L, y) \tag{41}$$

$$\bar{v}_x(x, L) = \bar{v}_x^{U,\exp}(x) = v_x^{U,\exp}(x) \tag{42}$$

$$\bar{v}_y(x, L) = \bar{v}_y^{U,\exp}(x) = v_y^{U,\exp}(x) \tag{43}$$

$$\bar{v}_x(x, -L) = \bar{v}_x^{D,\exp}(x) = v_x^{D,\exp}(x) \tag{44}$$

$$\bar{v}_y(x, -L) = \bar{v}_y^{D,\exp}(x) = v_y^{D,\exp}(x). \tag{45}$$

A set of equations is then obtained by projecting the boundary conditions in Fourier sine and cosine series for $n > 0$ (Einstein convention is used for repetition of indices):

$$\bar{v}_n^{x,R} = \Big(D_1^n + (a_n + L)D_2^n\Big)e^{-\frac{n\pi}{2}} + \Big(-D_3^n + (a_n - L)D_4^n\Big)e^{\frac{n\pi}{2}} \tag{46}$$

$$\bar{v}_n^{x,L} = \Big(D_1^n + (a_n - L)D_2^n\Big)e^{\frac{n\pi}{2}} + \Big(-D_3^n + (a_n + L)D_4^n\Big)e^{-\frac{n\pi}{2}} \tag{47}$$

$$\bar{v}_n^{y,U} = \Big(A_1^n + (a_n + L)A_2^n\Big)e^{-\frac{n\pi}{2}} + \Big(-A_3^n + (a_n - L)A_4^n\Big)e^{\frac{n\pi}{2}} \tag{48}$$

$$\bar{v}_n^{y,D} = \Big(A_1^n + (a_n - L)A_2^n\Big)e^{\frac{n\pi}{2}} + \Big(-A_3^n + (a_n + L)A_4^n\Big)e^{-\frac{n\pi}{2}} \tag{49}$$

$$\begin{aligned}\bar{v}_m^{y,R} = &\Big(a_n A_2^n + A_1^n\Big)d_{nm} + A_2^n e_{nm} + \Big(a_n A_4^n - A_3^n\Big)f_{nm} - A_4^n g_{nm} + \\ &+ A_2^0 b_m + \Big[\Big(D_1^n + D_2^n L\Big)e^{-\frac{n\pi}{2}} + \Big(D_3^n + D_4^n L\Big)e^{\frac{n\pi}{2}}\Big]c_{nm}\end{aligned} \tag{50}$$

$$\begin{aligned}\bar{v}_m^{y,L} = &(-1)^n\Big[\Big(a_n A_2^n + A_1^n\Big)d_{nm} + A_2^n e_{nm} + \Big(a_n A_4^n - A_3^n\Big)f_{nm} - A_4^n g_{nm}\Big] + \\ &+ A_2^0 b_m + \Big[\Big(D_1^n - D_2^n L\Big)e^{\frac{n\pi}{2}} + \Big(D_3^n - D_4^n L\Big)e^{-\frac{n\pi}{2}}\Big]c_{nm}\end{aligned} \tag{51}$$

$$\begin{aligned}\bar{v}_m^{x,U} = &\Big[(A_1^n + A_2^n L)e^{-\frac{n\pi}{2}} + (A_3^n + A_4^n L)e^{\frac{n\pi}{2}}\Big]c_{nm} + \Big[(D_1^n + a_n D_2^n)d_{nm} + D_2^n e_{nm} + \\ &(a_n D_4^n - D_3^n)f_{nm} - D_4^n g_{nm}\Big] + D_2^0 b_m\end{aligned} \tag{52}$$

$$\begin{aligned}\bar{v}_m^{x,D} = &\Big[(A_1^n - A_2^n L)e^{\frac{n\pi}{2}} + (A_3^n - A_4^n L)e^{-\frac{n\pi}{2}}\Big]c_{nm} + (-1)^n\Big[(D_1^n + a_n D_2^n)d_{nm} + D_2^n e_{nm} + \\ &(a_n D_4^n - D_3^n)f_{nm} - D_4^n g_{nm}\Big] + D_2^0 b_m,\end{aligned} \tag{53}$$

and for $n = 0$:

$$\bar{v}_0^{x,R} = 2D_1^0 + 2D_2^0 L \tag{54}$$

$$\bar{v}_0^{x,L} = 2D_1^0 - 2D_2^0 L \tag{55}$$

$$\bar{v}_0^{y,U} = 2A_1^0 + 2A_2^0 L \tag{56}$$

$$\bar{v}_0^{y,D} = 2A_1^0 - 2A_2^0 L, \tag{57}$$

and the 4 additional conditions for $\bar{v}_0^{x,U}$, $\bar{v}_0^{x,D}$, $\bar{v}_0^{y,R}$, $\bar{v}_0^{y,L}$ are approximately satisfied by continuity of the velocity at the corners of the rectangle. In the equations 46 to 53, we have introduced

the coefficients

$$c_{nm} = \frac{2n[-1+(-1)^{m+n}]}{\pi(n^2-m^2)} \text{ for } m \neq n, c_{nn} = 0 \quad (58)$$

$$d_{nm} = \frac{2n[-e^{-\frac{n\pi}{2}}+(-1)^m e^{\frac{n\pi}{2}}]}{(n^2+m^2)\pi} \quad (59)$$

$$e_{nm} = 2L\frac{[m^2(2-n\pi)-n^2(2+n\pi)]e^{-\frac{n\pi}{2}}-(-1)^m[n^2(n\pi-2)+m^2(2+n\pi)]e^{\frac{n\pi}{2}}}{[(n^2+m^2)\pi]^2} \quad (60)$$

$$f_{nm} = \frac{2n[(-1)^{(1+m)}e^{-\frac{n\pi}{2}}+e^{\frac{n\pi}{2}}]}{(m^2+n^2)\pi} \quad (61)$$

$$g_{nm} = 2L\frac{[n^2(n\pi-2)+m^2(2+n\pi)]e^{\frac{n\pi}{2}}+(-1)^m[m^2(n\pi-2)+n^2(2+n\pi)]e^{-\frac{n\pi}{2}}}{[(n^2+m^2)\pi]^2} \quad (62)$$

$$b_n = \frac{4L[1-(-1)^n]}{(n\pi)^2}, \quad (63)$$

and the Fourier coefficients of the boundary conditions

$$\bar{v_n}^{x,R/L} = \frac{1}{L}\int_{-L}^{L} dy \bar{v}_x^{R/L,\exp}(y)\cos\frac{n\pi(y-L)}{2L} \quad (64)$$

$$\bar{v_n}^{y,R/L} = \frac{1}{L}\int_{-L}^{L} dy \bar{v}_y^{R/L,\exp}(y)\cos\frac{n\pi(y-L)}{2L} \quad (65)$$

$$\bar{v_n}^{x,U/D} = \frac{1}{L}\int_{-L}^{L} dx \bar{v}_x^{U/D,\exp}(x)\cos\frac{n\pi(x-L)}{2L} \quad (66)$$

$$\bar{v_n}^{y,U/D} = \frac{1}{L}\int_{-L}^{L} dx \bar{v}_y^{U/D,\exp}(x)\cos\frac{n\pi(x-L)}{2L} \quad (67)$$

To obtain the unknown constants A^n, D^n the system of linear equations 46 to 57 is solved numerically for $0 \leqslant n \leqslant N$. In practice we choose $N = 100$.

2.3. **Comparison to two-dimensional experimental flow profiles.** To compare theoretical flow profiles with experimentally measured velocity profiles, we assumed $\eta/\eta_b = 1$. We then adjusted the normalised force exerted by ppl cells, f/η_b. We found that values of f/η_b reported in Table 1 accounted well for 2D experimental profiles obtained in wild-type and in *slb* mutants. In *slb* mutants, the force exerted by ppl was decreased by 20%, in accordance to the decrease in relative velocity between ppl cells and neurectoderm (Table 1).

As in section 1.2, we then can estimate the ratio η_b/ξ from the value of f/η_b and the value of f/ξ. A characteristic hydrodynamic length can be defined from this ratio by:

$$l_2 = \sqrt{\eta_b/\xi}. \tag{68}$$

Note that although we expect l_1 and l_2 to have similar order of magnitude, these two lengths are not equal in general as l_2 is defined from the 2D bulk viscosity of the fluid, while l_1 is defined from an effective one-dimensional viscosity. We report in Table 1 a value of $l_2 \simeq 133\mu$m.

To estimate a corresponding physical value of friction against the ppl cells, one would need an estimate of the neurectoderm viscosity η_b. Since we are not aware of direct measurements, we estimate it from $\eta_b \sim \eta_{3D} h$ with η_{3D} the tissue 3D shear viscosity and h the width of the neurectoderm. Using measurements of zebrafish deep-cell viscosities $\eta_{3D} \simeq 10^3$Pa.s [1] and $h \simeq 20\mu$m, we arrive at $\eta_b \simeq 2 \cdot 10^4 Pa.s.\mu$m and $\xi \simeq 1$Pa.s.μm^{-1}.

3. Determination of geometrical parameters

3.1. **Determination of geometrical parameters.** We discuss here the determination of geometrical parameters of the theoretical description. Geometrical parameters were measured at 70% epiboly.

- The initial position of the leading edge of ppl cells relative the margin, along the dorsal midline of the embryo, was measured in each experiment. In addition, ppl cells velocity was acquired over time by cell tracking. By integrating the ppl cell AV velocity over one hour time frame, we calculated the overall displacement of ppl cells over this period. By using their initial position, we were able to pinpoint the location of the leading edge at the end of the considered time frame. From this average position we then extracted the value of y^{ppl}.
- The length L^E was set according to experimental measurements of the distance from the animal pole to the EVL boundary measured at 70% epiboly. Its value in each experiment is given in Table 2.
- The lengths L_x^{ppl} and L_y^{ppl} are obtained from measurements of the size of the domain covered by ppl cells and are reported in Table 2.

Exp	R (μm)	L^E (μm)	L_x^{ppl} (μm)	L_y^{ppl} (μm)	y^{ppl} (μm)	L (μm)
wt	350	670	50	90	320	175
slb	350	590	50	90	373	175

Table 2. Values of the geometrical parameters used for the plots in Fig.5. Lengths are reported at 70% epiboly.

- We also report in Table 2 the size of the measurement domain L used for comparison between theory and experiment.

References

[1] H. Morita, S. Grigolon, M. Bock, G. S. Krens, G. Salbreux & C.-P. Heisenberg, Developmental Cell 40, no. 4 (2017): 354-366.